N73-13960

NASA CONTRACTOR REPORT

NASA CR-2170

NASA CR-2170

BOILING INCEPTION IN TRICHLOROTRIFLUOROETHANE DURING FORCED CONVECTION AT HIGH PRESSURES

by R. S. Dougall and T. E. Lippert

Prepared by
UNIVERSITY OF PITTSBURGH
Pittsburgh, Pa. 15213
for Lewis Research Center

NATIONAL AERONAUTICS AND SPACE ADMINISTRATION • WASHINGTON, D. C. • DECEMBER 1972

1. Report No. NASA CR-2170	2. Government Accession No.	3. Recipient's Catalog No.

4. Title and Subtitle BOILING INCEPTION IN TRICHLOROTRIFLUOROETHANE DURING FORCED CONVECTION AT HIGH PRESSURES	5. Report Date December 1972 6. Performing Organization Code
7. Author(s) R. S. Dougall and T. E. Lippert	8. Performing Organization Report No. None 10. Work Unit No.
9. Performing Organization Name and Address University of Pittsburgh Pittsburgh, Pennsylvania 15213	11. Contract or Grant No. NGL 39-011-079 13. Type of Report and Period Covered Contractor Report
12. Sponsoring Agency Name and Address National Aeronautics and Space Administration Washington, D.C. 20546	14. Sponsoring Agency Code

15. Supplementary Notes

Project Manager, Yih-Yun Hsu, Physical Science Division, NASA Lewis Research Center, Cleveland, Ohio

16. Abstract

The inception of bubbles during forced convection was studied experimentally by using trichlorotrifluoroethane (R-113 or Freon-113). The experiments were performed in a rectangular channel, 12.7 × 9.5 mm in cross section. Heating was from a 3.2 mm wide strip embedded in the longer side of the channel. The pressures studied ranged from 3.6 to 20.7 bar, mass velocities from 0.70×10^3 to 6.00×10^3 kg m^{-2} s^{-1}, and inlet subcoolings from 26 to 97 °C. Photographs of the flow were used to determine when bubbles first appeared on the heated surface. These data were compared with wall temperature measurements and inception theories. A reasonable method for calculating the complete boiling curve was found to agree with these results.

17. Key Words (Suggested by Author(s)) Two-phase flow Flow boiling Freon-113 Incipience of boiling	18. Distribution Statement Unclassified - unlimited

19. Security Classif. (of this report) Unclassified	20. Security Classif. (of this page) Unclassified	21. No. of Pages 57	22. Price* $3.00

* For sale by the National Technical Information Service, Springfield, Virginia 22151

BOILING INCEPTION IN TRICHLOROTRIFLUOROETHANE DURING FORCED CONVECTION AT HIGH PRESSURES

by R.S. Dougall and T.E. Lippert

University of Pittsburgh

SUMMARY

The inception of bubbles during forced convection was studied experimentally using Refrigerant-113 (FREON) as the fluid. The experiments were performed in a rectangular channel, 12.7 x 9.5 mm in cross section. Heating took place by electrical dissipation from a 3.2 mm wide strip embedded in the longer side of the channel. The pressure range studied was from 3.6 to 20.7 bar, mass velocities from 700 to 6000 kg m^{-2} s^{-1}, and inlet subcoolings of 26 to 97 C.

Photographs of the flow were used to determine when bubbles first appeared on the heated surface. The heat flux corresponding to the conditions when bubbles first appeared were compared to thermodynamic theories of bubble inception. It was found that these heat fluxes were higher than those predicted by inception theories which is to be expected from an adequate theory. Furthermore, it was found that the effect of subcooling in these theories was so large under the conditions studied that assuming the vapor behaved as an ideal gas or assuming that the slope of the saturation pressure-temperature curve was a constant produced no significant change in the results. However, modifying the temperature field by a Prandtl number correction was not completely successful.

Wall temperature measurements were obtained under some of the test conditions. These data showed that under fully-developed turbulent flow in the test section, the heat transfer coefficients were found to be about 60 per cent higher than those calculated from correlations for circular tubes. Similar results have been reported by other investigators for rectangular geometries. A correlation was developed which predicted the single-phase turbulent convective heat transfer to ± 10 per cent.

The wall temperature data further established that it was possible to predict the boiling curve (heat flux versus wall superheat) from bubble inception out to fully-developed boiling data. The limited data obtained showed that this method was accurate to ± 20 per cent.

INTRODUCTION

Boiling heat transfer has come under considerable interest in recent years because of the many engineering applications in which high heat-transfer rates are required at modest temperature differences. Applications include such systems as nuclear reactors and rocket motors where heat transfer rates of the order of 500 to 5000 kW m^{-2} are common. Boiling is also important in boilers, evaporators, and more recently in the cooling of high-speed computer components. In this last example, the heat fluxes are modest, but the requirement of a reasonably uniform heated surface temperature is achieved by operating under boiling conditions in the cooling channels (ref. 1). The performance of each of these systems depends extensively on the heat-transfer process. Higher performance from existing systems is an economical necessity, and with the continual development of new systems, there is a need for the continual broadening of the engineer's understanding of all aspects of the boiling heat-transfer process.

One of the areas that has not been adequately described is that of subcooled flow boiling. There are several distinct heat transfer regions involved in the flow of a subcooled liquid through a heated channel. At low wall superheats, the heat transfer rate is governed mainly by single phase forced convection. The heat transfer coefficient is generally close to that for single-phase forced convection. As the wall superheat increases, the heat transfer is determined by the combined effects of forced convection and surface boiling. Heat transfer rates can be obtained that are several times higher than those predicted for non-boiling conditions. The parameters that influence the boiling curve in this region have not been entirely defined. At still higher wall superheats, the effects of forced convection seem to disappear and a single curve independent of velocity and subcooling is reached. This heat-transfer region is called fully-developed boiling. A schematic representation of these various regimes is shown in Figure 1.

The beginning of boiling (bubble inception) initiates a two-phase flow structure which will alter the pressure-drop and heat-transfer characteristics in a flow channel. The designer therefore must have a reliable means of predicting the onset of boiling in a given system. The basic mechanism that governs bubble inception is generally agreed upon, but several theoretical models have been developed that are based on slightly different approaches and assumptions. Most of the data used to test the various models has been with water as the fluid. The data obtained in this investigation consists of wall temperature measurements and photographs of the flow structure at or near inception with an organic liquid rather than water. The fluid is refrigerant-113 (also known as Freon-113 , Genetron-113, and trichlorotrifluoroethane) which will be tested over a reasonably wide range of pressures, flow rates, and subcoolings. The reason this fluid was chosen was the experimental facilities were available for experimental work with this fluid. Also, this fluid offers many advantages as a fluid for modeling water or liquid metal boiling systems since it has a low critical pressure and small latent heat.

BUBBLE INCEPTION THEORIES

The first appearance of bubbles on the heated surface initiates the onset of the ebullition process. The physical mechanism of nucleation is generally agreed upon. Bubbles originate from small gas-filled cavities that exist on the heated surface. The basic model is embodied in the Helmholtz and Clausius-Clapeyron equations and requires mechanical and thermodynamic equilibrium across the bubble interface. The equations are:

$$\Delta p = p_g - p_f = \sigma\left[\frac{1}{R_1} + \frac{1}{R_2}\right] \tag{1}$$

$$\frac{dp}{dT} = \frac{h_{fg}}{v_{fg}}\,\frac{1}{T}, \tag{2}$$

where R_1 and R_2 are the principle radii of curvature of the bubble and dp/dT is the rate of change of saturation pressure with saturation temperature. Thermal equilibrium requires that the vapor and liquid temperatures be equal, i.e., $T_g = T_f$.

Mechanical equilibrium is expressed by the Helmholtz equation, equation (1), and requires that the forces across the bubble interface balance. This equation shows that the bubble pressure (p_g) is greater than the liquid pressure. Since the temperatures of the vapor and liquid are equal and since the vapor must be at a saturation temperature corresponding to its pressure, the liquid must be superheated with respect to the pressure. This excess temperature in the liquid is related to the pressure by the Clausius-Clapeyron equation, equation (2). For a bubble shape approximating that of a spherical segment, equation (1) is written:

$$\Delta p = \frac{2\sigma}{r}, \tag{3}$$

where r is the bubble radius. Integrating and eliminating the pressure differences between equations (1) and (3) results in an expression between the excess superheat in the liquid and the bubble radius at thermostatic equilibrium. At the critical excess temperature T_{cr} corresponding to the critical bubble radius r_{cr}, the bubble begins to grow and will subsequently depart from or collapse at the heated surface. The mechanism of bubble growth and departure has been treated by Zuber, (ref. 2) Griffith, (ref. 3) Koumoutosos et al. (ref. 4). The criterion for initiating the ebullition process and a discussion of some of the surface parameters is given here.

The nature of the active nucleation sites on a heating surface has been given considerable analytical and experimental attention. Bankoff (ref. 5) has shown that bubble nucleation within the homogeneous liquid or at flat or projecting solid surfaces requires superheat-vapor-pressure differences of the order of magnitude of hundreds of atmospheres, much larger than experimentally observed. Many studies indicate that nucleation will preferentially occur at non-wetted cavity sites. Westwater et al. (ref. 6) report that after examining the boiling surface under a microscope during ebullition, in general, bubbles do originate from cavities or scratches on the surface. Not all cavities will serve as nucleation centers, since in some it is not possible to trap vapor. Bankoff (ref. 7) gives criteria to characterize cavities as to their ability to trap vapor. This depends to a large extent on the contact angle between the bubble interface and solid wall. This angle is determined by the static force balance between the surface tension forces of the vapor, liquid, and solid at the bubble interface and wall. Very steep cavities and re-entrant cavities from which complete displacement of vapor is not possible are generally good nucleating sites. Griffith and Wallis (ref. 8) suggest that the specification of a single dimension (cavity radius) is sufficient for characterizing an active nucleation site and that equations (2) and (3) are substantially correct. Furthermore, they conclude that the surface in the vicinity of a cavity is much cooler than elsewhere. They report that the surface conditions can have a profound effect on the gross nucleation characteristics of the heating surface, but that there does not appear to be significant differences between engineering surfaces, insofar as departure size or shape of the bubble is concerned. They further indicate that the cavity geometry and contact angle will effect its stability as a nucleation site but not the temperature at which a cavity will nucleate. They conclude that re-entrant cavities are very stable and very likely serve as the nucleation site for the initiation of boiling. Kurihara and Meyers (ref. 9) report that smooth surfaces tend to retard nucleation and suggest that in such systems bubble formation could result from minute explosions of highly superheated fluid. Degassing the liquid prior to boiling tests tends to retard bubble nucleation, while it has been found that it is easier to maintain boiling and obtain reproducible readings from paraffin-treated surfaces than from clean ones. (ref. 8) This latter observation is attributed to some contact angle effect on cavity stability. Stability was also found to be quite sensitive to the way in which the boiling was started. Jontz and Meyers (ref. 10) have reported on the effect of addition of surface active agents on ebullition. Addition of such agents reduce the surface tension of the solutions, and in this way the effect of surface tension on bubble formation is studied. Two effects are reported. First, a decrease in the dynamic surface tension results in an increase in the boiling coefficient and, secondly, in a solution of Aerosol* and water, a four-fold increase in the boiling coefficient but no change in the dynamic surface tension. This second result is attributed to the effect of the detergent increasing the number of active nuclei. Gaertner and Westwater (ref. 11) have photographed the heating surface during boiling and have correlated the active site density to the heat flux. They report that the inception of boiling (as determined from photographs) does not occur at the knee in the boiling curve.

Each of the above mentioned studies (and many not specifically cited) have contributed to the understanding of the basic process which influences bubble nucleation, but the problem remains to relate the basic surface parameters to the heat transfer in some quantitative manner. To this end, the work of Hsu, (ref. 12) Han and Griffith, (ref. 13) Bergles and Rohsenow, (ref. 14) and Frost and Dzakowic (ref. 15) are reviewed. In these studies an attempt is made to establish a relationship between the cavity radius, wall temperature, and heat-transfer rate to determine the range of cavity sizes that qualify as active sites and to predict the onset of boiling.

Each of the above mentioned inception models are developed from the same basic equation and physical mode; i.e., bubbles originate from gas-filled cavities and begin to grow when conditions exist such that there is a net heat flux into the bubble. The solution of this heat transfer problem is complex and the criteria of a net heat flux is stated simply as a certain condition on the fluid and bubble temperatures. Thus, solution of the problem requires obtaining expressions for the respective temperatures.

The liquid temperature profile in the vicinity of the heated surface is taken to be linear, i.e.,

$$T_f = T_w - (\Delta T_w) \frac{y}{\delta_l} \tag{4}$$

---

[*] See ref. 10.

or in terms of the wall heat flux,

$$T_f = T_w - q'' \frac{y}{k} = T_b + \frac{q''}{h} - \frac{q''}{k} y \tag{5}$$

where, in equation (4) δ_1 is a distance proportional to the thickness of the thermal boundary layer and q" is the wall heat flux. Such linear temperature profiles have been measured near the wall in boiling systems. (ref. 16 & 17)

The approach in obtaining a solution is to determine the bubble temperature by first integrating equation (2) and then eliminating the pressure of the vapor, p_g, using equation (1) (or equation (3)). From the resulting equation for bubble temperature, T_g is a function of the physical properties of the liquid and a characteristic dimension of the bubble such as cavity or bubble radius. The form of this equation is basically the same for all the different models and may be written:

$$T_g = T_s \left(1 + \frac{A}{r_c}\right) \tag{6}$$

where A is a constant for a given fluid and system pressure, and r_c is the cavity radius. The constant A having the dimensions of length is in part a grouping of fluid properties where the particular properties appearing in the grouping depend on the model being considered. The exact forms of equation (6) for the different models are summarized below.

Hsu (ref. 12) and also Han and Griffith, (ref. 13) in determining T_g approximate dp/dT by $(p_g - p_f)/(T_g - T_s)$, neglect the vapor density in comparison to that of the liquid and obtain the particular form of equation (6)

$$T_g = T_s \left[1 + \frac{1}{C_2}\left(\frac{1}{\rho_g}\right) \frac{2\sigma}{h_{fg}\, r_c}\right] \tag{7}$$

C_2 is a constant which accounts for the shape of the bubble. Hsu assumes a truncated sphere while Han and Griffith and the others take the bubbles to be hemispherical, i.e., $C_2 = 1$. A hemispherical bubble at a cavity mouth has the minimum radius of curvature for the bubble. Bergles and Rohsenow (ref. 14) develop their model from an extension of Hsu and Graham's (ref. 18) work. They start with the Clausius-Clapeyron equation in differential form; assume that the vapor behaves as an ideal gas and neglect the vapor density in comparison to that of the liquid. After integrating and combining with the Helmholtz equation they obtain for the bubble temperature, after assuming that the product $T_g \cdot T_s$ is approximately equal to T_s^2;

$$T_g - T_s = \left[\frac{T_s^2 R_g}{h_{fg}}\right] \ln \left[1 + \frac{2\sigma}{r_c p_f}\right] \tag{8}$$

where R_g is the gas constant. An approximate form of equation (8) is

$$T_g = T_s \left[1 + \left(\frac{R_g T_s}{p}\right) \frac{2\sigma}{h_{fg} r_c}\right] \tag{9}$$

This approximation is good when $\frac{2\sigma}{r_c p} << 1$ which is generally true. In equation (7), the term ρ_g was an approximation for $1/V_{fg}$ for the case of low pressure where $\rho_g << \rho_f$. Frost and Dzakowic (ref. 15) found that the original Clausius equation could be integrated directly since over a broad range of pressures,

$$\frac{h_{fg}}{v_{fg} T_s} \cong \text{Constant.} \tag{10}$$

The equation for bubble temperature becomes,

$$T_g = T_s \left[1 + \left(v_{fg}\right) \frac{2\sigma}{h_{fg} r_c}\right] \tag{11}$$

Returning to the general formulation for T_g, equation (6), a graphical representation of this equation and also the liquid temperature profile, equation (5), is shown in Figure 2. For a given fluid and fixed flow rate, bulk temperature and pressure, the heat transfer coefficient h is fixed. This fixes the intercept of the fluid temperature profile line with the $T = T_b$ line. The variables that remain are T_w, q", and r_c. According to the basic model, bubbles will nucleate and grow only if there is a net heat flow into the vapor. This criteria for nucleation is simply stated as a condition on the liquid and vapor temperatures: that the two temperatures be equal at a certain distance above the heated surface. This distance is generally taken equal to or proportional to the cavity radius, depending on the model being considered, i.e.,

$$T_g = T_f \qquad \text{at } y = \lambda\, r_c \tag{12}$$

where λ is a parameter whose functional form may differ with the different models as discussed below.

Bergles and Rohsenow (ref. 14) assume this distance to be one bubble radius ($\lambda = 1$) but indicate that in all probability this represents an upper limit, since all the surrounding fluid is then able to transfer heat to the bubble. Han and Griffith (ref. 13) determine that this distance is 3/2 the bubble radius. Their argument is based on establishing the isothermal line that passes through the top point of the bubble as determined from potential flow theory and the fluid flow analogy. Hsu (ref. 12) assumes it is a constant, C_1, which is a function of contact angle and cavity geometry. However, for a typical value he suggests 1.25. Frost and Dzakowic (ref. 15) claim the distance to be proportional to the square of the Prandtl number, ($\lambda = Pr^2$) arguing that in any thermal boundary layer the Prandtl number dictates the shape of the temperature profile.

Returning to Figure 2, it is clear that the shape of the fluid temperature line is given by specifying either the wall temperature, T_w or the heat flux, q". Equation (12) is satisfied whenever the fluid temperature line intersects the T_g curve as illustrated by the line labeled $q'' > q''_{incp}$. In general, two solutions for r_c are obtained; i.e., a quadratic equation results. Any cavities laying outside the range of the two solutions are ineffective nucleating sites, while those sizes laying within the range are effective but not necessarily actives sites.

Boiling inception corresponds to the minimum heat flux at which bubbles first appear. This corresponds to the fluid temperature line of minimum slope that still intersects the T_g curve, i.e., when the fluid temperature line falls tangent to the T_g curve.

Algebraically, this means equal roots in the quadratic expression for r_c, i.e., that the discriminant be equal to zero. Combining equations (5) and (6) under the conditions given in equation (12) gives the following equation for the maximum and minimum cavity size.

$$\frac{hr_c}{k} = \frac{1}{2\lambda}\left(1 - \frac{h\Delta T_{sub}}{q''}\right) \pm \sqrt{\frac{1}{4\lambda^2}\left(1 - \frac{h\Delta T_{sub}}{q''}\right)^2 - \frac{hT_s}{q''\lambda}\left(\frac{hA}{k}\right)} \quad (13)$$

Equal roots require

$$\left(1 - \frac{h\Delta T_{sub}}{q''}\right)^2 = \frac{4\lambda hT_s}{q''}\left(\frac{hA}{k}\right) \quad (14)$$

Solving equation (14) for q" (which is now q''_{incp}) again results in a quadratic equation. The root with the negative sign on the radical corresponds to the solution in the second quadrant where wall temperature (T_w) is less than the fluid saturation temperature. This solution has no physical meaning in the present boiling system and is therefore discarded. Thus, the inception heat flux becomes,

$$q''_{incp} = h\left[\Delta T_{sub} + 2\lambda T_s\frac{hA}{k} + \sqrt{\left(\Delta T_{sub} + \lambda T_s\frac{hA}{k}\right) 4\lambda T_s\frac{hA}{k}}\right] \quad (15)$$

The sum of the second and third terms in equation (15) gives the value of wall superheat necessary for bubble inception. Thus,

$$\Delta T_{sup} = 2T_s\left(\frac{h\lambda A}{k}\right) + \sqrt{\left(\Delta T_{sub} + T_s\frac{h\lambda A}{k}\right) 4\, T_s\frac{h\lambda A}{k}} \quad (16)$$

The expressions used by the various authors for A and λ are given in Table I. These expressions will be discussed in more detail after the results of the exprimental program are derived.

EXPERIMENTAL APPARATUS

The R-113 was contained in a closed loop system and circulated using a canned rotor, centrifugal pump. The pump delivered a head in excess of 5 bar. The main loop piping was 25.4 mm diameter type 304 stainless steel tube. A schematic of the loop is shown in Figure 3.

As shown, the flow would proceed from the pump through the lines into a horizontal preheater (item 2). The preheater had the capability of producing a total of 25 kw of power. This power was provided by five Chromolox immersion heaters, each with a rated output of 5 kw at 240 Volts. Four of the heaters were connected as either simply on or off, depending on the amount of heat needed. The remaining heater was connected to a variable transformer and used for the fine control.

From the preheater, the flow would divide and some pass through a standard A.S.M.E. venturi flow measuring meter (item 3) and then through the main throttling valve and into the test section (item 4) while the latter flow proceeds through a by-pass line (item 5) and then rejoins the test section flow prior to entering the coolers. The quantity of flow entering the test section was controlled by the throttling valve on the by-pass line and with the main throttling valve which was located upstream of the entrance of the test section. This arrangement permitted adjustment of the pressure drop taken at the test section.

After rejoining, the flow would enter two helical concentric tube single pass heat exchangers (item 6). Cooling water was provided directly from the city line and controlled with a valve. From the coolers, the R-113 flow would enter the suction side of the pump. A Sporlan high water capacity filter (item 7) was incorporated on a by-pass line at the suction side of the pump.

The system pressure was maintained by a separate pressurizing unit that had a capacity of about 21 liters (item 8). The fluid in this unit was maintained at saturation by heating it, using a 5 kw Chromolox immersion heater whose power output was controlled with a variable transformer. The liquid level in the pressurizer was monitored by visual observation through a sight gage (item 9). The unit was controlled automatically by a temperature controller (Assembly Products Model 429). A bourdon tube gage 0-70 bar was used to measure the loop system pressure at the outlet of the pump. Pressure at the suction side of the pump was also monitored.

Provided on the loop were two safety relief valves. One was a 48 bar blowout disk (item 10). The second was a pressure regulator relief valve that could be set to any pressure up to 27 bar (item 11).

The test section was a 1.32 meter long rectangular duct 12.7 by 9.5 mm through which R-113 (Trichlorotrifluoroethane) was circulated and heated from one side wall. A photograph of the section assembly is shown in Figure 4. The duct was vertically orientated in the flow loop with the R-113 flowing against gravity. The channel assembly consisted of an inlet transition section, a heated section, and an unheated exit section. The transition section extended approximately 45 diameters upstream of the heated portion of the test section and was designed to allow a smooth flow transition from the 25.4 mm diameter circular tubing to the rectangular geometry of the duct. The transition section helped to dampen out flow disturbances that were caused by pipe fittings and allowed for a fully-developed velocity profile at the beginning of the heated length. The heated section was 0.526 m long and of the same rectangular geometry as the transition section. The exit section extended approximately 28 diameters downstream of the exit of the heated length.

The test section assembly was constructed from a 140 bar stainless steel sight gage so visual observation of the flow was possible. This was accomplished by slightly modifying the side window construction of the sight gage. Actually, the windows had been constructed from two separate pieces of glass, as seen from the fanned view of the section assembly in Figure 5. The 3.2 mm thick inside pieces of glass formed the two opposite side walls of the channel. Each of these pieces of glass had been chemically pre-stressed for high tensile strength to resist cracking at high temperature. The 19 mm thick back support pieces were high pressure gauge glass. These pieces sealed the section by pressing against gaskets made of Durabla when the steel frames of the housing were tightly bolted together. There were two viewing windows on each of the two sides of the duct, each measuring 32 mm by 350 mm. The third wall of the duct corresponds to the inside portion of the sight gage. The fourth side, the heated wall of the duct, contained a stainless steel strip, 3.2 mm wide, 0.80 mm thick, and 510 mm long imbedded in and bonded to a 6.4 mm thick piece of fibrous impregnated plastic insulating material (Lamitex). The insulation was in turn bonded to the sight gage wall. The heating strip was also brazed at both ends to small brass support blocks. Copper electrodes were threaded into each of these supports. The electric power was supplied by a continuous duty selenium rectifier with a rated dc output of 18 volts, 200 amperes. The electrical leads to the heating strip were passed through the test section housing wall by employing Conax pressure glands that threaded into the steel housing.

Actually, three different stainless steel heating strips were tested. Each was of the same geometry, but with two of them, thermocouples had been attached to the back side of the strip in an effort to obtain the temperature of the heated wall surface. In one case, the thermocouples were tack welded directly to the back of the strip, while in the second design the thermocouples were press fitted against the back of the strip but electrically insulated from it by a 0.127 mm thick strip of mica. (This design proved inadequate.) The third design had no thermocouples attached to the heating strip.

The test section assembly and adjacent piping were insulated prior to testing with several layers of 50 mm thick spun fiberglass (except for the glass window portion of the test section). This minimized the heat loss from the section assembly. The heat loss from the back side of the stainless steel strip was calculated to be less than one percent.

The basic measurements made on the test section include: section pressure, the inlet and outlet centerline fluid temperature, flow rate of the R-113, and the voltage and current through the heating strip. From these measurements all the system variables and test quantities were calculated or derived. An estimate of the error involved in these measurements is given below. The subsequent cumulative effect of these errors on the derived quantities is given in the Error Analysis section, Appendix A.

The test section pressure was measured from a 3.2 mm tap located approximately 127 mm from the inlet of the heated portion of the duct. This pressure was recorded with a Bourbon type pressure gage 0-500 psi in 5 psi sub-division, U.S. Gauge Model Number 19011. The gage had been calibrated using a double area dead weight tester. The gage could be read to a ± 0.07 bar accuracy. This is not the accuracy at which the system pressure is known because the temperature in the loop pressurizing unit was a quasi-equilibrium situation. With careful operation and some practice, however, the pressurizing unit could be trimmed so that the system pressure could be maintained and read to within the following tolerances:

$$P = 9.45 \pm 0.14 \text{ bar}$$

$$P = 13.1 \pm 0.21 \text{ bar}$$

$$P = 20.7 \pm 0.28 \text{ bar}$$

Temperatures of the bulk fluid at the inlet and exit of the channel were obtained using calibrated, commercially purchased iron-constantan thermocouples. They were ungrounded, had a stainless steel sheath (1.59 mm OD), and a guaranteed nominal accuracy of $\pm$ 1.1°C. A calibration using an oil bath arrangement showed that the accuracy of these thermocouples could be taken as $\pm$ 0.6°C over the temperature range encountered in this investigation.

The wall temperature measurements were made using thermocouples constructed from commercially purchased number 26 gauge iron-constantan wire. The calibration of these thermocouples had to be made in place (attached to the heating strip) and over a limited temperature range (25-100°C) using the above described commercially purchased thermocouples as reference. The calibration results indicated the accuracy to be within ± 1.1°C, except with one of the wall thermocouples. The data from this thermocouple (T_7) has been omitted. The location of the thermocouples

from the started of the heated length is given in Table II.

All thermocouple outputs were connected through a selector switch and ice bath assembly to a Leeds and Northrup Model 8686 precision portable potentiometer. The reading accuracy of this instrument was taken as 0.0005 millivolts or approximately 0.1°C.

The flow through the test section was measured using either a standard ASME venturi meter with a 6.85 mm throat or a standard ASME 6.60 mm sharp-edged orifice. Both devices were calibrated with the usual weight tank arrangement. The following equations represent the best fit curves to the calibration data:

$$C_v = 0.954 \left(1 - \frac{2990}{Re_v}\right) \quad \text{Venturi}$$

$$C_o = 0.605 \left(1 + \frac{423}{Re_p}\right) \quad \text{Orifice}$$

The respective data and curves are shown in Figures 6 and 7. The maximum uncertainty in the discharge coefficient in either case was taken as ± 3 percent.

The venturi or orifice pressure drop (as the case may be) was measured using a 70 inch well type mercury manometer with 0.10 inch graduations. The manometer could be read to ± 0.025 inch. During test runs, a slight oscillating of the mercury occurred which frequently negated this accuracy. In these cases, the maximum uncertainty in the mercury height was taken to be less than ± 2.5 percent.

The power to the test section heating strip was calculated from measurements of voltage and current. Voltage was measured using a direct current precision type PX-4, 1000 ohms/volt voltmeter with a rated accuracy of 0.5 percent of the full scale reading.

Measurements of the voltage drop at increments along the heating strip length were made. This data for two different heat flux values are plotted in Figure 8. Results indicate the expected linear profile, i.e., uniform heat flux.

The current to the test section was determined by measuring the voltage drop across a precision shunt rated at 50 millivolts per 300 amperes, ± 1/2 percent. The readings were made using a potentiometer similar to that used in measuring the temperatures. Actually, some variation in the current of the heating strip was obtained during the tests. The maximum uncertainty in the current reading was estimated to be within ± 2.5 percent.

All photographs were obtained using a Nikon Automatic Reflex Photomic 35 mm camera with the Medical-Nikkor fixed focus master lens. Six auxiliary lens were available and could be attached singly or in pairs to the master lens. This allowed for a wide range of reproduction ratios. Best pictures were obtained with the reproduction ratios 1.5X and 2X (object fields of 0.67 x 0.98 and 0.47 x 0.71, respectively) and F-stop numbers of 45 and 32. The combination of these parameters yielded a depth of field that could be varied from approximately 0.81 mm (F = 32, 2X) to about 2.77 mm (F = 45, 1.5X). The photographs were taken on Kodak 35 mm Tri-X Pan, Fast Black and White film (ASA-400).

The photographic subjects, in this case the R-113 bubbles, were back lighted using a General Radio type 1431-A Electronic Strobotac. The strobotac operated in synchronization with the camera shutter, both being triggered by a 10-second delay timer that is built into the camera. The high intensity (11 million beam candelas), short duration (3μ second) flash from the strobotac was diffused by a piece of frosted glass that was located between the light source and test section.

EXPERIMENTAL PROCEDURE

The following test procedure was observed during the course of the data acquisition. First, instrumentation was set up, balanced, and the camera and flash unit mounted at the test section. The loop was then filled, pressurized to test conditions, and checked for leaks. Next, the loop pump was started and the R-113 allowed to circulate through the Sporlon filter for a minimum of fifteen minutes. This procedure was repeated prior to beginning each test day.

After the above preparations, the loop parameters were set to the particular test conditions. First, the flow rate was adjusted to its approximate value and the test section pressure drop fixed to an acceptable value. Both these settings were made by throttling the main valve at the inlet of the test section and the valve on the by-pass line. Controlling the pressure drop at the test section allowed for optimum use of the coolers and heaters and prevented vapor from being generated at the suction side of the pump. The temperature of the bulk R-113 was brought to the desired value. This was accomplished by turning on the loop preheater and allowing the liquid temperature to increase in small increments. Once the desired temperature was attained, a final adjustment was made on the flow rate. The loop was now operating at a quasi-equilibrium condition that was suitable for data acquisition. The above outlined procedure took approximately three hours.

Once the system was operating at equilibrium, the thermocouples located at the inlet and exit of the test section were calibrated. This involved recording the millivolt output of each thermocouple while the test section was in the power-off condition, i.e., no power to the heating strip. This calibration was repeated both prior and immediately following a test run. Also, this procedure was repeated if during the course of the day the flow rate or fluid temperature was set to a new value.

Test runs lasted from eight to ten hours. Data was obtained (approximately) on an alternate day basis for a two-month period. During this time, the R-113 was changed three times, each time being replaced by a new or recently distilled batch.

FORCED CONVECTION NON-BOILING RESULTS

The recorded test data is listed in Table III and includes measurements of the heat flux from the wall, inlet and outlet bulk temperature, system pressure, and the wall temperature at seven positions along the length of the wall. Originally, eight thermocouples had been provided, but apparently, thermocouple number seven (located at L = 409 mm from the beginning of the heated inlet) broke when the test section was assembled. The thermocouples had been tack welded to the back side of the heating strip. The calculation of the expected heat loss from the back side of the strip and the subsequent temperature drop across its thickness is given in ref. 19. The heat loss was found to be negligible, and the surface temperature was calculated from the thermocouple readings by subtracting the temperature drop across the heating strip.

The local heat transfer coefficients h, and subsequent Nusselt numbers Nu, were calculated from

$$h = q''/(T_w - T_b) \tag{17}$$

and

$$Nu = hd_e/k \ . \tag{18}$$

The approximate error in each of the measured and calculated quantities is given in Appendix A. The maximum errors in the heat transfer coefficient and Nusselt number are about 9 and 20 percent, respectively. For the forced convection data reported herein, the flow is turbulent, and since the entrance length to the beginning of the heated section is approximately 40 diameters, (see Experimental Apparatus,) the velocity profile can be taken as fully developed (ref. 20).

Typical wall temperature profiles are presented in Figure 9 and indicate the expected temperature variation with axial length (neglecting for a moment thermocouples number 3 and 4) in a developing thermal boundary layer and uniform heat flux. A quantitative description of the thermal entrance effect is obtained by plotting the ratio of the local to exit Nusselt number against the heated length, as shown in Figure 10. The Nusselt numbers are the averaged values. Ignoring once more the data corresponding to thermocouple numbers 3 and 4, a relatively smooth curve may be drawn through the remaining points. This curve shows that high heat transfer rates exist at the inlet but decrease with length, and within 150 mm or 13 diameters the temperature distribution is developed. This data is in good agreement with the data of Hartnett (ref. 21) and the work of Deissler (ref. 22) who report entrance lengths of 15 diameters at Reynolds numbers of 10^5, decreasing to 6 diameters at Reynolds numbers of 10^4. It is unclear from the present data to what extent the thermal entrance depends on Reynolds number. The solid line shown in the figure is indicative of the overall data, and no attempt was made to account for the varying Reynolds numbers.

The anomaly in the data at locations 3 and 4 cannot be entirely explained. It is noted, however, that this deviation occurs at a physical location along the test section channel corresponding to a partition that separates the two adjacent viewing windows, see Figure 4 and 5. Although there exists no large identifiable abrupt flow interruptions at this point, there does exist a transition in hardware material, from glass side walls to steel, back to glass with slight discontinuities at the side walls. This steel section is about 50 mm long and corresponds to that length between location 3 and 4 in Figure 10. The data at this point shows increased heat transfer rates. This is probably occurring because of local flow disruptions arising at the interface of the adjoining pieces of hardware. The data shows, however, that once past this section the profile curve of the heat flux adjusts in the expected fashion, as shown by the dotted curve. The net effect is a shifting of the entrance section and a fully-developed flow in this test section cannot be assumed before 300mm (25 diameters).

A correlation of the heat transfer results at the fully-developed conditions (location number 8) is shown in Figure 11. The data is given in ref. 19. Dimensional analysis and a least square fit of the data result in the following equation:

$$Nu = 0.0578 \, Re^{0.762} \, Pr^{0.4} \left(\frac{\mu_b}{\mu_w} \right)^{0.14} \tag{19}$$

The dimensionless groupings were evaluated at bulk temperature. The exponent on the Prandtl number and viscosity ratio were taken in accordance with the commonly used turbulent heat transfer correlations. The resulting equation is in general agreement with equations for turbulent flow in tubes. However, the curve is shifted probably due to the rectangular geometry and unsymmetric heating.

EXPERIMENTAL RESULTS FOR BOILING

Two types of experimental data were obtained concerning the bubble inception point in subcooled forced convection boiling of R-113. In the first set of data, wall temperature measurements were obtained for varying conditions of heat flux, mass velocity, subcooling, and pressure. This information is shown in Table III. The second set of data consisted of photographs of the flow in the test section for various values of heat flux, mass velocity, subcooling, and pressure. The photographs are of a region between 400 to 500 mm from the start of the heated length. A typical photograph of the flow before inception is shown in Figure 12, and one after inception is shown in Figure 13. Additional photographs of the flow can be seen in ref. 19. The results of this photographic investigation are shown in Table IV. The heat fluxes listed in this table are those corresponding to the first photograph in which bubbles appeared on the surface. However, if the bubble population was very large, these values were not used as inception values and it was assumed that the inception heat flux was missed by a large amount. The photographs are approximately a factor of ten magnification of the real dimensions of the test section. The diameters of the bubbles obserbed on the photographs are on the order of a hundred microns.

DISCUSSION OF RESULTS

The theoretical predictions of the inception heat flux all have the form given in equation (15). The only differences are in the way the fluid property function, A, is calculated and in the way the critical cavity radius is scaled to the distance on the wall, i.e. the value of λ. The various schemes used by the authors of references (12) through (15) are shown in Table I. The values of the fluid property function were calculated over a range of pressures for R-113. The results are shown in Figure 14.

The procedure of Frost and Dzakowic (ref. 15) give the smallest values of A. The values calculated by Hsu (ref. 12) and Han and Griffith (ref. 13) are identical to each other and very close to those obtained by Frost and Dzakowic. This is understandable since the only time there will be significant differences is when the specific volume of the liquid is becoming of the same order of magnitude as the specific volume of the vapor. These specific volumes become equal at the critical pressure which is equal to 34.4 bar for R-113. At a pressure of 25 bar, the value of A used in ref. 12 and 13 is only 20% higher than the value of ref. 15.

The procedure of Bergles and Rohsenow (ref. 14) gives the highest values of A. They are only a few percent higher than those of Frost and Dzakowic at atmospheric pressure. This difference increases to around 15% at 5 bar and then to around 50% at 15 bar. However, the general trend of the fluid property function is to decrease rapidly as the pressure increases. In fact, it drops by two decades on log paper when the pressure increases from 1 to 25 bar. This rapid decrease means that the value of A will have a smaller effect on the inception heat flux given by equation (15).

It turns out that the choice of the value for λ can be much more important. In particular, the choice for λ used by Frost and Dzakowic, the square of the Prandtl number has a very strong influence for R-113 since its Prandtl number is about 7. This result is shown graphically in Figures 15 and 16. In these figures, the inception heat flux and wall superheat are presented as functions of pressure. The flow rate is assumed to be that which would give a heat transfer coefficient of 4.00 $\mathrm{kWm^{-2}\,^{o}C^{-1}}$, a typical value for the system studied.

Three theoretical curves are presented for two different values of fluid subcooling, 30°C and 60°C. Also shown on Figure 15 are the asymptotic values of the heat flux when the superheat goes to zero. These values are: 119 $\mathrm{kW\,m^{-2}}$ for 30°C subcooling and 239 $\mathrm{kW\,m^{-2}}$ for 60°C subcooling. The Frost and Dzakowic theory is presented twice, once with the Prandtl number scaling and once without it. When the Frost and Dzakowic theory is not scaled with the square of the Prandtl number, it turns out to give values nearly identical to those of Bergles and Rohsenow. This is true even at pressures around 20 bar where the fluid property function used by Bergles and Rohsenow is 50% higher than that used by Frost and Dzakowic. When the Prandtl number correction is applied, the wall superheats increase by about a factor of ten. The inception heat fluxes also increase, substantially more at low pressures than at higher pressures. Also, the greater the subcooling, the less is the effect of the Prandtl number correction.

The authors of ref. 15 derived their Prandtl number correction from a study of pool boiling data. They probably never intended for their result to be applied to forced-convection boiling without some experimental verification. The experimental data obtained with a Prandtl number of around 7.0 is being used.

It would appear that the Prandtl number correction proposed by Frost and Dzakowic is too severe for forced-convection boiling of R-113 since extremely high superheats are predicted as shown in Figure 16. It would also seem that the correction proposed by

Hsu (ref. 12) and Han and Griffith (ref. 13) are not very large. The order-of-magnitude of their results should be about the same as that between the theory of Bergles and Rohsenow (ref. 14) and that of Frost and Dzakowic (ref. 15) with the Prandtl number correction. As can be seen from Figures 15 and 16, this is a relatively minor difference. Therefore, the theories of Hsu and Han and Griffith will not be discussed further.

A comparison between the inception theories of Bergles and Rohsenow (ref. 14) and Frost and Dzakowic (ref. 15) with the photographic data is shown in Figure 17. The experimental data used is that presented in Table IV. Since the data presented in Table IV is the heat flux at which bubbles first appeared in the photographs of the heated surface, these experimental values should be somewhat higher than the actual inception values. Therefore the data points should be below the forty-five degree line on Figure 17. All except one of the data points calculated using the theory of Bergles and Rohsenow (ref. 14) fulfill this criteria. The data points calculated using the theory of Frost and Dzakowic (ref. 15) fall above the forty-five degree line except for the 20.7 bar data. This is to be expected from the results shown on Figures 15 and 16.

The data taken at 9.45 bar and 13.1 bar seem to agree with each other. However, the higher pressure data, 20.7 bar, is significantly lower. There are two possible causes of this result. First, the bubbles at 20.7 bar are extremely small and are difficult to detect on the photographs. This could mean that a somewhat larger heat flux beyond the inception value is needed to detect the bubbles. Second, the fluid properties at these pressures are not as well known. This could also tend to make this data more uncertain.

The real question of how good are the theories can be satisfactorily answered when their use in predicting heat transfer from a boiling surface is considered. The inception point on a boiling curve such as Figure 1 indicates the point beyond which the resulting heat transfer will start to be influenced by the presence of bubbles on the surface. This is an asymptotic effect which is negligible at the inception point but grows rapidly. For this reason, it is impossible to predict the inception point with great accuracy. However, having a good theory for predicting the inception point allows one to develop a reasonable correlation for the heat transfer in the local boiling region (the region where boiling and forced covection both influence the heat transfer).

Bergles and Rohsenow (ref. 14) have developed a correlation for predicting heat transfer in the local boiling region. Two pieces of information are required to use this result. First, a correlation for single-phase forced convection is needed. This is available as equation (19) for the present system. Second, a correlation for fully-developed boiling is needed. This is available from the work of Panian (ref. 23). His equation for the fully-developed boiling heat transfer coefficient is

$$h_{fbd} = 0.149(q'')^{0.65}\ p^{\ 0.55} \tag{20}$$

where the heat transfer coefficient is in kW m^{-2} K^{-1}; the heat flux is in kW m^{-2}; and the pressure is in bars. This equation was developed for the forced-convection boiling of R-113 from a stainless steel surface between the pressures of 10.0 to 17.5 bar. Although the pressure range is slightly high for some of the data obtained, this equation will be used for lack of anything better.

Bergles and Rohsenow (ref. 14) suggest the following equation to represent the complete boiling curve after bubble inception.

$$q'' = q''_{fc} \left\{1.0 + \left[\frac{q''_{fdb}}{q''_{fc}} \left(1 - \frac{q''_{bi}}{q''_{fdb}}\right)\right]^2\right\}^{1/2} \tag{21}$$

This curve gives the wall heat flux if the wall temperature and bulk fluid temperatures are given. The force-convection heat flux, q''_{fc}, is given by the equation

$$q''_{fc} = h_{fc}\ (T_w - T_b) \tag{22}$$

where h_{fc} is the heat-transfer coefficient given by equation (19).

The fully-developed boiling heat flux, q''_{fdb} is given by the equation

$$q''_{fdb} = h_{fdb}\ (T_w - T_s) \tag{23}$$

where h_{fdb} is the heat-transfer coefficient given by equation(20)

The heat flux, q''_{bi}, is the value of the heat flux on the fully-developed boiling curve taken at the inception wall superheat, i.e.

$$q''_{bi} = h_{fdb}\ (T_w - T_s)_{incp} \tag{24}$$

This last bit of information accounts for the influence of bubble inception. Wall superheats are correlated using equation (16) with λ=1.0 and A given by reference 15.

Equation (21) has a value equal to the forced-convection heat flux at bubble inception. As the wall superheat increases beyond this value, the contribution due to boiling increases. The curve merges asymptotically into the fully-developed boiling curve at high superheats, i. e. when $q''_{fdb} \gg q''_{fc}$.

A great deal of difficulty occurred during attempts to obtain wall temperature measurements in the test section used for this study. This was mainly due to the geometry of a heated strip imbedded in an insulating wall. Differential thermal expansion tended to cause the strip to lift out of the insulation. This made it hard to keep thermocouples in good thermal contact with the back of the strip. However, one of the test sections had thermocouples silver soldered to the back of the heating strip. After some effort (see ref. (19)), this test section gave meaningful wall temperature readings. These are the results shown in Table III.

A comparison between equation (21) and the data of Table III that contain boiling points is shown in Figures 18 and 19. It can be seen equation (21) does a reasonable job of predicting the boiling curve in the region of local boiling. Figure 20 shows a comparison between the theoretical location of the point of bubble inception and the location of the photographic points where bubbles were visible for the first time. Bubble inception was calculated using the theory of Frost and Dzakowic (ref. 15), but without the Prandtl number correction. The pressure is 13. 1 bar. As can be seen on the figure, the first visible bubbles appear somewhere between the theoretical bubble inception and the fully-developed boiling curve. This is probably as good as can be expected owing to the asymptotic nature of bubble inception.

CONCLUSIONS

In this report, theoretical predictions of bubble inception were compared with experimental data for the forced-convection boiling of Refrigerant-113 at pressures from 3. 6 bar to 20. 7 bar. Bubble inception was determined by photographing the flow in the test section and determining the conditions for which bubbles first appeared on the photographs. These results were compared with existing theories leading to the following conclusions:

1. All the theories lead to essentially the same magnitude of inception heat flux and wall superheat unless a large scaling parameter is used to relate bubble radius to distance from the wall. If the scaling by the Prandtl number squared is used, the resulting values of inception heat flux and wall superheat are too high for R-113 which has Prandtl number of around 7. 0.

2. The inception theories that assume the vapor behaves as a perfect gas give results very close to those theories that used values from tables of thermodynamic properties. This is fortunate because these theories can be used for fluids where the thermodynamic properties are not readily available in table form.

3. Accurate experimental determination of the bubble inception point is not possible due to the asymptotic behavior of the flow at this point. The first visual observation of bubbles occurs at heat fluxes somewhat greater than inception values.

4. An empirical correlation of the heat transfer in the local boiling region agreed with the experimental data to within ± 20 per cent.

APPENDIX A

ERROR ANALYSIS

The data from any experiment can only be interpreted within the limits of the accuracy and reliability of the measurements. These limits are difficult and often impossible to ascertain in single sample experiments. Nevertheless, it is necessary for the experimenter to attempt to describe the uncertainties in the data in order to add credence to the results. Such an analysis would first be extremely helpful in selecting the apparatus best suited for the experiment, and secondly, give the experimenter a basis for evaluating his data.

An analysis has been conducted to describe the uncertainties in the data reported herein. The calculations are based on the equations presented by Kline and McClintock (ref. 24), who show that the uncertainty interval W_r in some function R of n independent variables V_i is given by

$$W_r = \left[\left(\frac{\partial R}{\partial V_1} W_1\right)^2 + \left(\frac{\partial R}{\partial V_2} W_2\right)^2 + \ldots + \left(\frac{\partial R}{\partial V_n} W_n\right)^2\right]^{1/2} \qquad (A.1)$$

where W_i is the uncertainty interval in the variable V_i. In developing the above equation, it was assumed that the same odds exist for each of the variable intervals and for the result, i.e., if the confidence intervals of the W_i variables are 90 percent, then the confidence interval on W_r will also be 90 percent. Using this equation, the uncertainty in the variables can be estimated. The basic measured quantities and their respective uncertainty intervals are summarized in Table A.1. The confidence intervals in the variables were arbitrarily set at 90 percent.

The calculations for the error in the derived quantities are summarized below.

(A) For the mass velocity G, the equation is written

$$G = KC\sqrt{Z},$$

where K is a constant dependent on the geometry of the metering device and the fluid properties, $K = K(\rho, D_h, D_1, D_2)$, C is the coefficient of discharge, and Z the mercury displacement in the

TABLE A.1

	Quantity	Symbol and Unit	Quantity Value and Confidence Interval (max.)
1.	Pressure	P (bar)	9.45 ± 0.14 bar
2.	Mercury displacement	Z (inch)	1.0 ± 0.05 inch
3.	Temperature difference	ΔT (^oC)	25 ± 5^oF
4.	Temperature	T (^oF)	100 ± 2^oF
5.	Voltage	V (volts)	10 ± 0.25 volts
6.	Current	A (amps)	50 ± 1.25 amps
7.	Length of heated strip	l (mm)	526 ± 6.3 mm
8.	Width of heated strip	b (mm)	3.18 ± 0.08 mm
9.	Channel width	w (mm)	12.70 ± 0.25 mm
10.	Channel height	a (mm)	9.50 ± 0.25 mm

manometer. Using Eq. (A.1), the uncertainty in G is written

$$\frac{W_G}{G} = \left[\left(\frac{W_K}{K}\right)^2 + \left(\frac{W_C}{C}\right)^2 + \left(\frac{1}{2}\,\frac{W_Z}{Z}\right)^2\right]^{1/2} \quad . \qquad (A.2)$$

K and C are not basic measured variables and their respective uncertainty interval must be derived. The uncertainty in the discharge coefficient C was determined from calibration data to be ± 3 percent, while the uncertainty in K was calculated by examining the functional relationship $K = K(\rho, D_h, D_1, D_2)$. The uncertainty in ρ, the fluid density and D_1 and D_2 the inlet and throat diameters of the venturi (or orifice) were taken to be small, compared to the uncertainty in D_h, the hydraulic diameter:

$$D_h = 2\frac{a \cdot w}{(a + w)} \quad .$$

The uncertainty in D_h using the values for the uncertainties in a and w from Table A.1 is (after applying Eq. (A.1)),

$$\frac{W_{D_h}}{D_h} = \pm\ 0.04\ ,$$

Thus, substituting the values for the uncertaintites of K, C, and Z into Eq. (A.2) yields the uncertainty in the mass velocity,

$$\frac{W_G}{G} = \pm\ 0.055\ .$$

This represents the maximum error. At the higher mass velocities this error is expected to reduce to around 5 percent, because the error in the manometer mercury displacement W_Z becomes small with increasing Z.

(B) For the heat flux, q", which is determined from voltage, amperage and geometry measurements, the equation is written:

$$q = \text{Constant} \cdot \frac{V\ .\ A}{b \cdot l}\ ,$$

where V is the voltage, A the amperage, and b and l are the width and length of the heating strip, respectively. The equation describing the uncertainty in q" is:

$$\frac{W_{q''}}{q''} = \left[\left(\frac{W_V}{V}\right)^2 + \left(\frac{W_A}{A}\right)^2 + \left(\frac{W_b}{b}\right)^2 + \left(\frac{W_l}{l}\right)^2\right]^{1/2}\ . \qquad \text{(A.3)}$$

Substituting for the uncertainty intervals of the basic measured quantities from Table A.1 into Eq. (A.3) yields:

$$\frac{W_{q''}}{q''} = \pm\ 0.036\ .$$

The uncertainty in b and l are fixed. Data indicates that the uncertainty in V and A remains approximately constant. Thus, the uncertainty $W_{q''}$ is reasonably insensitive to change in q".

(c) The error in ΔT_{sub} is the composite error in T_s and T_b. The local bulk temperature T_b at some given point in the channel was calculated from measurements of the inlet temperature and an energy balance, while the saturation temperature, T_s, was determined from the system pressure measurement and saturation tables.

The local bulk temperature could be calculated from

$$T_b = T_{in} + \frac{x}{L} (T_{out} - T_{in}) \quad . \tag{A.4}$$

The increase in the channel bulk temperature, as represented by the last term in the above equation, was always small compared to T_{in} (less than 10 percent). Thus, even a substantial error in the last term would not be significantly reflected in the sum. The error in determining the local bulk temperature T_b was therefore assumed to be that error associated with the bulk inlet temperature, T_{in}, i.e., $\pm$ 0.6°C. To find the uncertainty in the saturation temperatures, it was first necessary to determine the error in the measurements of the system pressure. Results are tabulated below.

$p = 9.45 \pm 0.14$ bar ; $T_s = 136 \pm 1.7^{\circ}C$

$p = 13.1 \pm 0.21$ bar ; $T_s = 154 \pm 1.7^{\circ}C$

$p = 20.7 \pm 0.28$ bar ; $T_s = 180 \pm 1.7^{\circ}C$

The error in the temperature difference ΔT_{sub} was calculated using Eq. (A.1). The bulk temperature was a basic test parameter and was varied in the different test runs. Thus, a minimum, medium, and maximum uncertainty was calculated,

$$\Delta T_{sub} = 97 \pm 1.8^{\circ}C \; ; \quad \frac{W_{\Delta T_{sub}}}{\Delta T_{sub}} = \pm 0.019 \text{ minimum,}$$

$$\Delta T_{sub} = 60 \pm 1.8^{\circ}C \; ; \quad \frac{W_{\Delta T_{sub}}}{\Delta T_{sub}} = \pm 0.030 \text{ medimum,}$$

$$\Delta T_{sub} = 25 \pm 1.8^{\circ}C \; ; \quad \frac{W_{\Delta T_{sub}}}{\Delta T_{sub}} = \pm 0.072 \text{ maximum.}$$

(D) For the Nusselt number defined as

$$Nu = \frac{hd_e}{k}$$

where h is the heat transfer coefficient, d_e the hydraulic diameter, and k the thermal conductivity. The uncertainty in Nu is given by:

$$\frac{W_{Nu}}{Nu} = \left[\left(\frac{W_h}{h}\right)^2 + \left(\frac{W_{D_h}}{D_h}\right)^2 + \left(\frac{W_k}{k}\right)^2\right]^{1/2} . \qquad (A.5)$$

The heat transfer coefficient h is obtained from:

$$h = \frac{q''}{(T_w - T_b)} .$$

The uncertainty in heat flux q", hydraulic diameter D_h, and the local bulk temperature T_b have been discussed above. The measurement of the wall temperature is discussed in Ref. 19. The overall uncertainty in T_w, is a combination of the calibration error (± 2 percent) and that due to heat loss (also about 2 percent). Thus,

$$\frac{W_{\Delta T_{w-b}}}{\Delta T_{w-b}} = \pm\ 0.04 .$$

The uncertainty in the thermal conductivity, k, has been reported to be of the order of ± 20 percent (Ref. 1). The uncertainty in the Nusselt number is therefore from Eq. (A.5).

$$\frac{W_{Nu}}{Nu} = 0.21.$$

(E) For the Reynolds number defined as

$$Re = \frac{Gd_e}{\mu}$$

the uncertainty is given by:

$$\frac{W_{Re}}{Re} = \left[\left(\frac{W_G}{G}\right)^2 + \left(\frac{W_{D_h}}{D_h}\right)^2 + \left(\frac{W_\mu}{\mu}\right)^2\right]^{1/2} \qquad (A.6)$$

The error in mass velocity, G, and hydraulic diameter, d_e, have been discussed. The uncertainty in the viscosity was taken as ± 10 percent. The uncertainty in the Reynolds number becomes

$$\frac{W_{Re}}{Re} = \pm\ 0.12\ .$$

This again represents the maximum error in the Reynolds number. When the mass velocity is increased (increasing Re), the uncertainty in the Reynolds number will decrease because the error in z decreases.

(F) For the Prandtl number,

$$Pr = \frac{\mu c_p}{k}$$

the uncertainty is

$$\frac{W_{Pr}}{Pr} = \pm\ 0.17$$

which represents only the contributions of the viscosity and thermal conductivity. The uncertainty in the specific heat, c_p, is ignored.

The above calculations represent an attempt to estimate the uncertainty in the measured and derived test quantities. The results should be considered only in a qualitative sense, since the actual errors of many of the variables are complicated functions of the variables themselves. The values reported above are the expected maximum uncertainties, and thus, most of the data should fall within these values.

APPENDIX B

SYMBOLS

A	fluid property grouping defined in Table I, m
C	constant, dimensionless
d_e	equivalent diameter, m
h	heat transfer coefficient, W m^{-2} K^{-1}
h_{fg}	latent heat of vaporization, J kg^{-1}
k	liquid thermal conductivity, W m^{-1} K^{-1}
Nu	Nusselt number based on equivalent diameter, dimensionless
p	pressure, N m^{-2}
P	pressure, N m^{-2}
Pr	Prandtl number, dimensionless
q''	heat flux, W m^{-2}
r	bubble radius, m
R	radius of curvature, m
Re	Reynolds number based on equivalent diameter, dimensionless
R_g	gas constant, J kg^{-1} K^{-1}
T	temperature, K
v	specific volume, m^{3} kg^{-1}
y	distance from the heated surface, m
δ_1	distance proportional to thermal boundary layer thickness,m
Δ	difference
λ	scaling parameter defined in Table I, dimensionless
μ	liquid viscosity, kg m^{-1} s^{-1}
ρ	density, kg m^{-3}
σ	surface tension, N m^{-1}

SUBSCRIPTS:

b	bulk
bi	bubble inception
c	cavity
cr	critical
f	saturated liquid
fc	forced convection
fdb	fully-developed boiling
fg	change from sat. liquid to sat. vapor

g	saturated vapor
incp	inception
o	orifice
s	saturation
sub	subcooling
sup	superheat
v	venturi
w	wall

REFERENCES

1. Bergles, A.E.; Bakhru, N.; and Shires, J.W.: Cooling of High-Power-Density Computer Components. Research Report No. 60, Dept. Mech. Eng., M.I.T., Nov. 1968.

2. Zuber, N.: Dynamics of Vapor Bubbles in Nonuniform Temperature Fields. Inter. J. of Heat and Mass Transfer, vol. 2, 1961, pp. 83-98.

3. Griffith, P.: Bubble Growth Rates in Boiling. Trans ASME, vol. 80, 1958, pp. 721-727.

4. Koumoutses, N.; Moissis, R.; and Spyridonos, A.: A Study of Bubble Departure in Forced Convection Boiling. J. of Heat Transfer, vol. 90,No. 2, May, 1968, pp.223-230.

5. Bankoff, S.G.: Ebullition from Solid Surfaces in the Absence of a Pre-Existing Gaseous Phase. Trans. ASME, vol. 79, 1957, pp. 735-739.

6. Westwater, J.W.; Clark, H.B.; and Strenge, P.S.: Active Sites for Nucleate Boiling. Chem. Engr. Prog. Symposium Series, vol. 55, 1959, pp. 103-110.

7. Bankoff, S.G.: Entrapment of Gas in the Spreading of a Liquid over a Rough Surface. AIChE Journal, vol. 4, no. 1, 1958, pp. 24-68.

8. Griffith, P.; and Wallis, J.D.: The Role of Surface Conditions in Nucleate Boiling. Chem. Engr. Prog. Symposium Series, vol. 56, no. 30, 1960, pp. 49-63.

9. Kurihara, M.H.; and Myers, J.E.: The Effect of Superheat and Surface Roughness on Boiling Coefficients. AIChE Journal, vol. 6, no. 1, 1960, pp. 83-91.

10. Jontz, P.D.; and Myers, J.E.: The Effect of Dynamic Surface Tension on Nucleate Boiling Coefficients. AIChE Journal, vol. 6, no. 1, 1960, pp. 34-38.

11. Gaertner, R.F.; and Westwater, J.W.: Population of Active Sites in Nucleate Boiling Heat Transfer. Chem. Engr. Prog. Symposium Series, vol. 56, no. 30, pp. 39-48.

12. Hsu, Y.Y.: On the Size Range of Active Nucleation Cavities on a Heating Surface. J. of Heat Transfer, vol. 84, no. 3, August 1962, pp. 207-216.

13. Han, C.Y.; and Griffith, P.: The Mechanism of Heat Transfer in Nucleate Pool Boiling. Research Report No. 7673-19, Dept. of Mech. Eng., MIT, 1962.

14. Bergles, A.E.; and Rohsenow, W.M.: The Determination of Forced-Convection Surface-Boiling Heat Transfer. J. of Heat Transfer, vol. 86, 1964, pp. 365-372.

15. Frost, W.; and Dzakowic, G.S.: An Extension of the Method for Predicting Incipient Boiling on Commercially Finished Surfaces. ASME Paper No. 67-HT-61, 1967.

16. Marcus, B.D.; and Dropkin, D.: Measured Temperature Profiles within the Superheated Boundary Layer above a Horizontal Surface in Saturated Nucleate Pool Boiling of Water. J. of Heat Transfer, vol. 87, 1965, pp. 333-341.

17. Lippert, T.E.; and Dougall, R S.: A Study of the Temperature Profiles Measured in the Thermal Sublayer of Water, Freon-113, and Methyl Alcohol During Pool Boiling. J. of Heat Transfer, vol. 90, 1968, pp. 347-352.

18. Hsu, Y.Y.; and Graham, R.W.: An Analytical and Experimental Study of the Thermal Boundary Layer and Ebullition Cycle in Nucleate Boiling. NASA TN D-594, 1961.

19. Lippert, T.E.: Experimental Determination of the Heat-Transfer and Vapor-Void Characteristics of R-113 in Subcooled Flow at Boiling Inception and at the Point of Net Vapor Generation. Ph.D. Thesis, Mech. Eng. Dept., Univ. of Pittsburgh, 1971.

20. Eckert, E.R.G.; and Irvine, T.F.: Incompressible Friction Factor, Transition and Hydrodynamic Entrance-Length Studies of Ducts with Triangular and Rectangular Cross Section. Proceedings of the Fifth Midwestern Conference on Fluid Mechanics, Univ. of Michigan, 1957, pp. 122-145.

21. Hartnett, J.P.: Experimental Determination of the Thermal Entrance Length for the Flow of Water and of Oil in Circular Pipes. J. of Heat Transfer, vol. 87, 1965, pp. 1211-1220.

22. Deissler, R.G.: Turbulent Heat Transfer and Friction in the Entrance Regions of Smooth Passages. J. of Heat Transfer, vol. 87, 1965, pp. 1221-1233.

23. Panian, D.J.: Subcooled Forced Convection Boiling of R-113 (FREON). M.S. Thesis, Mech. Eng. Dept., University of Pittsburgh, 1970.

24. Kline, S.J.; and McClintock, F.A.: Describing Uncertainties in Single Sample Experiments. Mech. Eng., Vol. 75, 1953, pp. 3-8.

TABLE I. - RELATIONS USED IN INCEPTION THEORIES

References	A	λ	$\lambda \cdot A$
Hsu (ref. 12)	$\frac{1}{C_2}\left(\frac{1}{\rho g}\right)\frac{2\sigma}{h_{fg}}$	C_1	$\frac{C_1}{C_2}\left(\frac{1}{\rho g}\right)\frac{2\sigma}{h_{fg}}$
Han & Griffith (ref. 13)	$\left(\frac{1}{\rho_g}\right)\frac{2\sigma}{h_{fg}}$	1.5	$1.5\left(\frac{1}{\rho g}\right)\frac{2\sigma}{h_{fg}}$
Bergles & Rohsenow (ref. 14)	$\left(\frac{R_g T_s}{p_f}\right)\frac{2\sigma}{h_{fg}}$	1.0	$\left(\frac{R_g T_s}{p_f}\right)\frac{2\sigma}{h_{fg}}$
Frost & Dzakowic (ref. 15)	$\left(v_{fg}\right)\frac{2\sigma}{h_{fg}}$	Pr^2	$Pr^2\left(v_{fg}\right)\frac{2\sigma}{h_{fg}}$

Suggested Values for C_1 and C_2 in ref. 12 are:

$C_1 = 2.00$, $C_2 = 1.25$

TABLE II.- LOCATION OF WALL THERMOCOUPLES

Thermocouple Number	Distance from Start of Heated Section (mm)
1	30
2	81
3	132
4	183
5	256
6	333
7	409 (broken)
8	485

TABLE III--EXPERIMENTAL WALL TEMPERATURE DATA

Run Number	System Pressure bar	Mass Velocity kg m^{-2} s^{-1}	Heat Flux kW m^{-2}	Bulk Inlet Temperature K	Bulk Outlet Temperature K	Wall Temperatures, K						
						T_1	T_2	T_3	T_4	T_5	T_6	T_8
1A	3.8	3.22×10^3	0	298.8	298.8	298.2	298.5	298.5	298.5	298.5	298.5	298.5
1B	3.8	3.22×10^3	24.9	300.8	300.9	306.0	307.3	306.5	306.2	307.7	307.7	308.7
1C	3.8	3.22×10^3	50.4	301.1	301.2	311.5	314.1	312.6	311.5	315.0	314.9	315.5
1D	3.8	3.22×10^3	89.7	301.2	301.2	316.7	324.4	321.3	319.4	325.5	325.5	325.9
1E	3.8	3.22×10^3	119.4	300.8	300.9	324.6	330.0	326.3	323.5	331.8	334.3	335.0
1F	3.8	3.22×10^3	204	301.6	301.7	341.4	349.8	344.0	339.5	353.2	357.7	358.8
1G	3.8	3.22×10^3	240	302.1	302.2	350.0	359.2	351.5	345.4	362.2	365.3	368.3
1H	3.8	3.22×10^3	299	301.7	301.8	359.0	366.9	358.7	351.9	370.7	371.9	374.9
1I	3.8	3.22×10^3	433	302.0	302.2	375.0	381.2	374.5	364.2	381.3	379.4	384.7
2A	3.6	1.72×10^3	20.2	302.4	302.4	309.2	311.0	309.9	309.5	310.8	311.4	311.3
2B	3.6	1.72×10^3	77.8	302.4	302.4	325.9	334.0	330.8	327.1	334.2	337.2	337.4
2C	3.6	1.72×10^3	118.4	302.4	302.5	336.7	349.2	344.0	337.0	349.4	353.0	353.4
2D	3.6	1.72×10^3	168.8	302.7	302.7	349.9	365.2	359.4	351.3	364.7	364.5	367.1
2E	3.6	1.72×10^3	224	302.8	302.9	362.2	369.5	376.2	360.8	373.2	372.5	375.1
2F	3.6	1.72×10^3	296	302.8	302.9	371.8	377.6	374.9	366.9	377.9	378.7	383.7
2G	3.6	1.72×10^3	376	302.9	303.1	377.8	380.5	379.4	373.3	382.6	383.3	386.3
2H	3.6	1.72×10^3	460	302.9	303.1	381.2	383.3	386.2	380.3	388.8	388.2	389.9
3A	6.9	3.98×10^3	20.3	302.7	302.7	306.2	307.5	307.5	306.4	311.1	313.8	--
3B	6.9	3.98×10^3	44.7	303.3	303.3	310.4	313.2	312.2	310.9	313.5	314.0	314.2
3C	6.9	3.98×10^3	78.7	303.4	303.4	315.6	320.5	319.3	317.0	321.4	322.5	322.9
3D	6.9	3.98×10^3	120.0	303.9	303.9	322.3	329.9	327.3	324.5	330.9	332.5	332.7
3E	6.9	3.98×10^3	170.2	304.1	304.1	329.2	341.0	337.5	333.3	343.7	344.9	344.4
3F	6.9	3.98×10^3	230	304.4	304.4	336.8	354.0	349.7	344.5	356.8	360.1	358.2
3G	6.9	3.98×10^3	303	304.8	304.8	344.7	368.2	361.8	354.9	371.9	376.7	371.2
3H	6.9	3.98×10^3	368	305.2	305.3	353.4	385.3	377.9	369.3	389.3	390.3	388.3
3I	6.9	3.98×10^3	448	305.4	305.5	362.6	398.0	390.4	381.0	399.8	398.6	401.2
4A	6.89	2.57×10^3	19.9	305.1	305.1	309.5	311.0	310.2	309.0	311.1	311.5	311.5
4B	6.89	2.57×10^3	44.4	305.3	305.4	314.5	318.0	316.7	314.1	318.5	319.5	319.8
4C	6.89	2.57×10^3	77.5	305.4	305.4	321.2	327.7	325.4	320.8	328.5	330.4	330.6
4D	6.89	2.57×10^3	120.0	305.6	305.7	329.3	339.8	336.8	329.7	341.5	344.8	344.2
4E	6.89	2.57×10^3	167.6	305.7	305.8	337.2	352.8	347.9	343.1	355.2	360.2	358.7
4F	6.89	2.57×10^3	224	305.9	305.0	346.5	369.2	363.5	358.4	373.4	375.2	375.8
4G	6.89	2.57×10^3	290	306.0	306.1	355.6	386.9	380.6	373.4	391.3	391.5	394.5
4H	6.89	2.57×10^3	364	306.2	306.3	368.1	399.4	393.4	385.2	401.4	400.9	402.5
4I	6.89	2.57×10^3	450	306.4	306.5	381.2	404.3	401.5	392.9	407.0	405.7	407.5
5A	6.89	3.95×10^3	0	310.5	310.5	310.7	310.7	310.3	310.3	309.9	309.9	309.9
5B	6.89	3.95×10^3	19.5	310.4	310.4	313.4	314.9	313.9	312.5	314.2	314.2	313.9
5C	6.89	3.95×10^3	43.7	310.6	310.6	317.1	320.2	318.8	315.9	319.5	320.1	319.8
5D	6.89	3.95×10^3	77.2	310.7	310.7	322.5	327.4	325.4	320.2	327.5	328.1	327.8
5E	6.89	3.95×10^3	118.8	310.6	310.6	328.6	336.0	333.4	328.8	337.0	338.0	337.6
5F	6.89	3.95×10^3	169.4	310.8	310.8	334.5	346.7	343.4	336.9	348.4	350.1	349.5
5G	6.89	3.95×10^3	225	310.8	310.9	341.2	358.3	353.8	347.1	361.4	363.9	363.3
5H	6.89	3.95×10^3	292	310.8	310.8	347.9	372.1	366.9	359.9	376.9	379.2	375.9
5I	6.89	3.95×10^3	364	310.8	310.8	354.8	386.4	380.8	370.5	390.5	391.1	392.1
5J	6.89	3.95×10^3	447	310.9	311.0	363.8	397.2	392.5	381.0	399.5	398.9	399.9
6A	6.89	3.90×10^3	19.6	329.0	329.0	332.2	333.5	332.7	329.5	333.0	333.0	332.9
6B	6.89	3.90×10^3	43.8	329.0	329.1	335.8	338.7	337.9	332.7	338.7	338.9	338.9
6C	6.89	3.90×10^3	76.5	329.0	329.0	340.5	345.2	343.7	335.9	345.7	346.2	346.0

TABLE III--EXPERIMENTAL WALL TEMPERATURE DATA (CONT'D)

Run Number	System Pressure bar	Mass Velocity kg m^{-2} s^{-1}	Heat Flux kW m^{-2}	Bulk Inlet Temperature K	Bulk Outlet Temperature K	Wall Temperatures, K						
						T_1	T_2	T_3	T_4	T_5	T_6	T_8
6D	6.89	3.90×10^3	117.1	329.3	329.3	345.9	353.2	350.9	340.0	354.4	354.8	354.6
6E	6.89	3.90×10^3	168.0	329.3	329.3	351.8	363.5	361.0	346.2	366.1	367.2	365.9
6F	6.89	3.90×10^3	224	329.4	329.4	357.9	374.5	371.2	357.5	378.3	373.0	378.5
6G	6.89	3.90×10^3	289	329.4	329.5	364.8	387.1	383.0	367.9	390.8	390.1	391.9
6H	6.89	3.90×10^3	367	329.4	329.5	374.1	396.8	393.9	376.0	399.2	399.6	400.4
6I	6.89	3.90×10^3	455	329.5	329.7	384.5	405.2	401.3	382.9	404.7	405.2	405.4
7A	6.89	3.33×10^3	77.5	296.0	296.0	307.2	312.8	310.8	307.7	312.5	313.3	--
7B	6.89	3.33×10^3	229	296.9	296.9	327.3	348.7	342.2	335.7	348.7	351.6	--
7C	6.89	3.33×10^3	367	296.1	296.2	339.5	378.5	370.7	358.4	380.4	381.7	--
7D	6.89	3.33×10^3	445	296.7	296.8	347.9	390.5	383.1	371.3	391.9	390.8	--
7E	6.89	3.33×10^3	537	296.9	297.0	358.3	397.3	392.2	380.3	399.0	396.7	--
7F	6.89	3.33×10^3	645	297.2	297.3	368.0	401.5	401.4	389.0	404.8	402.5	--
7G	6.89	3.33×10^3	777	297.4	297.5	374.7	405.8	414.0	398.4	409.9	413.9	--

TABLE IV. - INCEPTION HEAT FLUX DATA

Run Number	Pressure Bar	Mass Velocity $kg\ m^{-2}s^{-1}$	Bulk Subcooling ^oC	Inception Heat Flux $kW\ m^{-2}$
1	9.45	813	30	53.0
2	9.45	1260	30	69.3
3	9.45	1260	53	127.5
4	9.45	1630	67	182.0
5	9.45	2710	33	157.9
6	13.1	773	44	75.3
7	13.1	1000	37	85.7
8	13.1	1000	57	87.0
9	13.1	1360	42	117.5
10	13.1	1360	33	86.0
11	13.1	2170	40	154.3
12	13.1	3050	41	208
13	13.1	5830	36	340
14	20.7	699	47	103.6
15	20.7	699	54	104.2
16	20.7	1180	46	125.0
17	20.7	2040	38	202
18	20.7	3600	26	150.0
19	20.7	3600	36	293

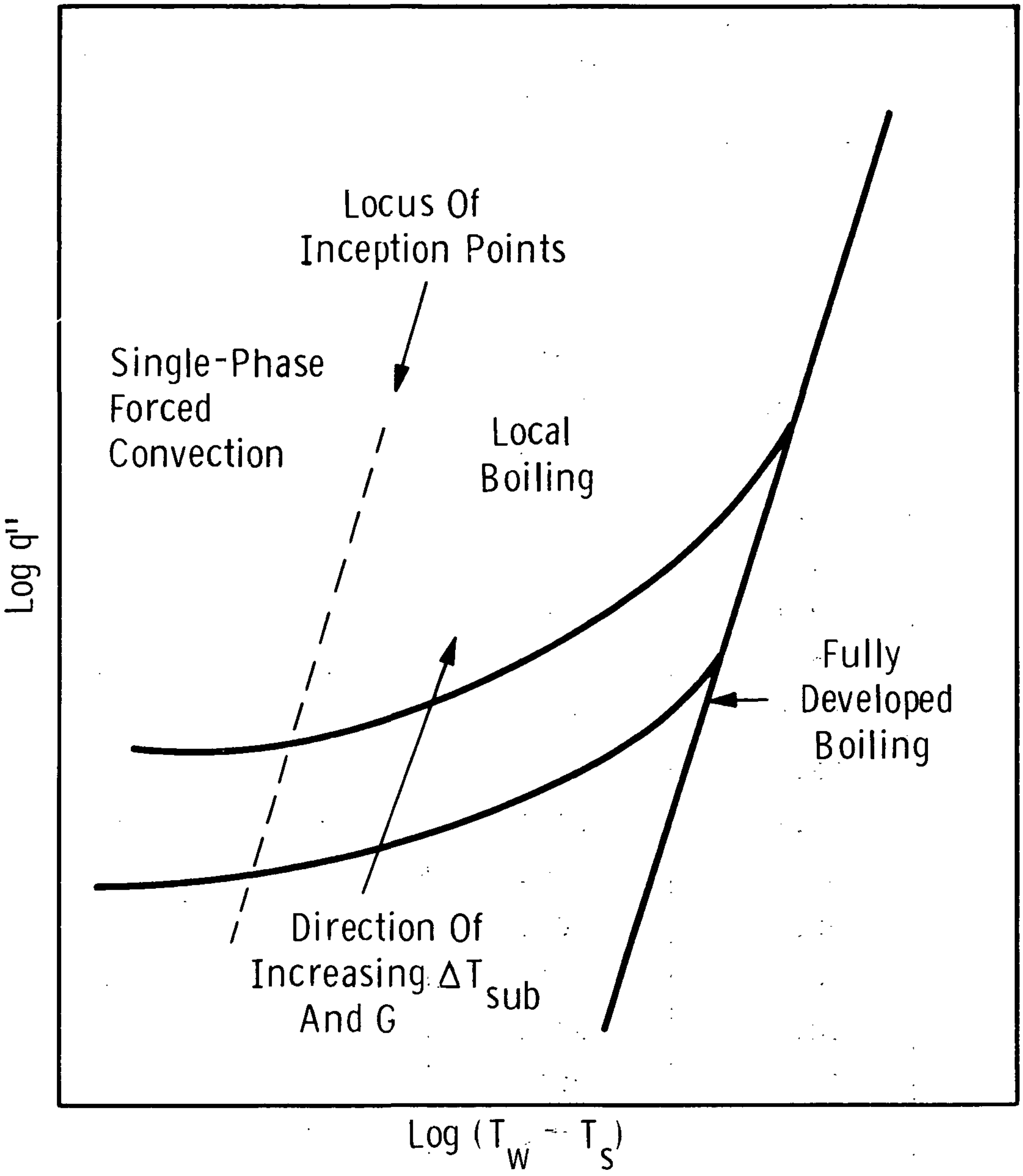

Fig. 1 Typical relation between wall heat flux and wall superheat in subcooled forced-convection boiling

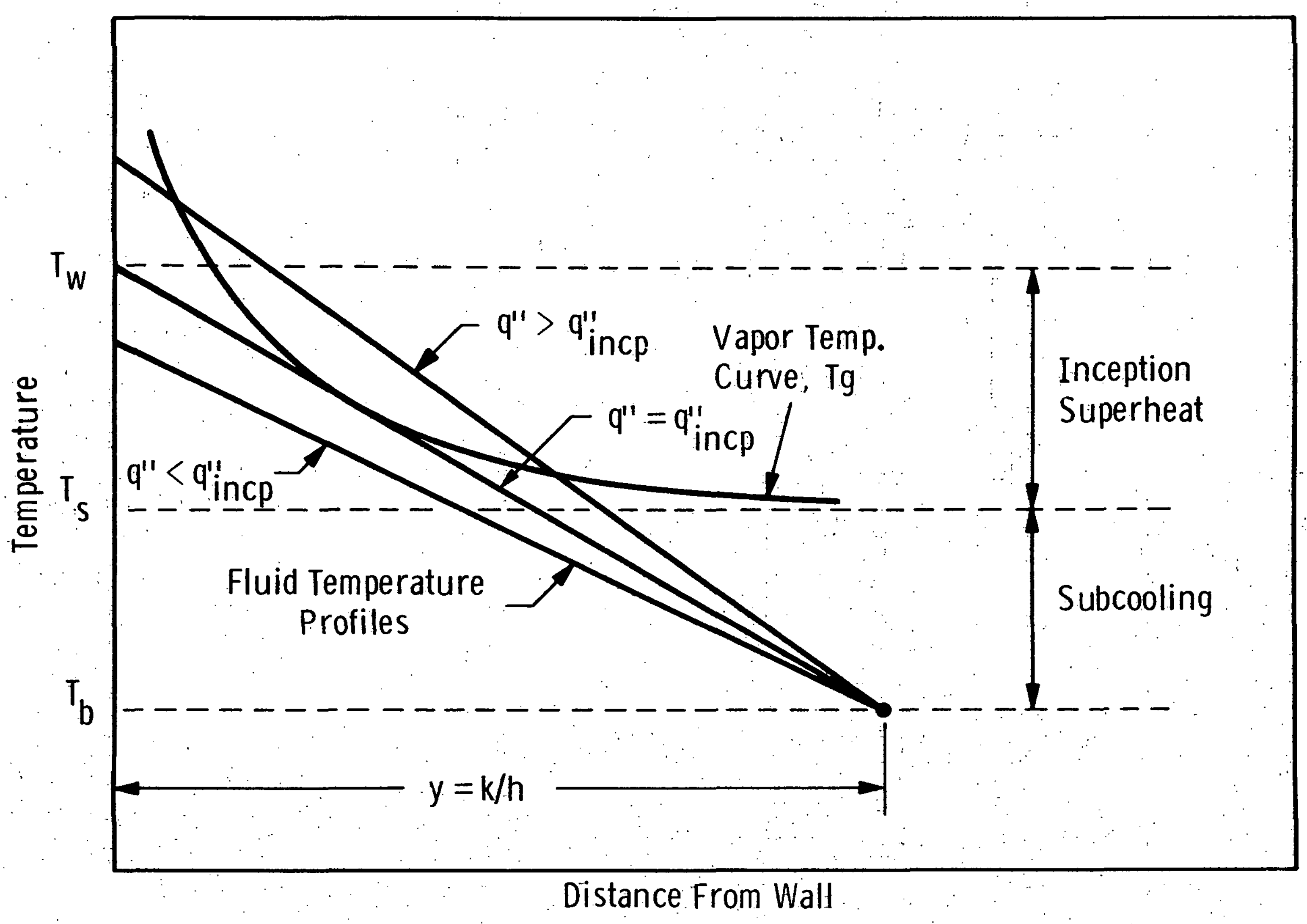

Fig. 2 Schematic representation of boiling inception

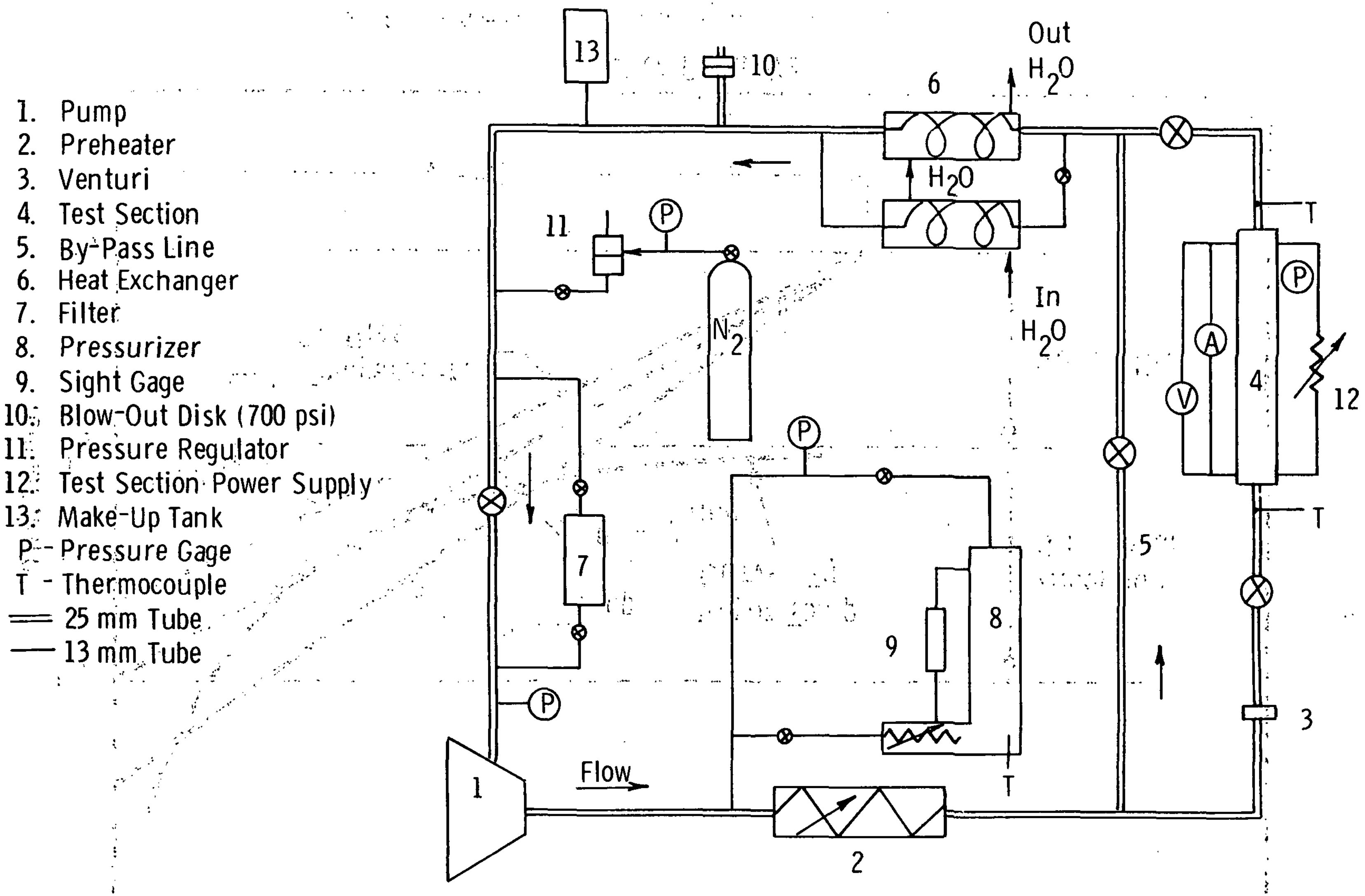

Fig. 3 Flow loop schematic

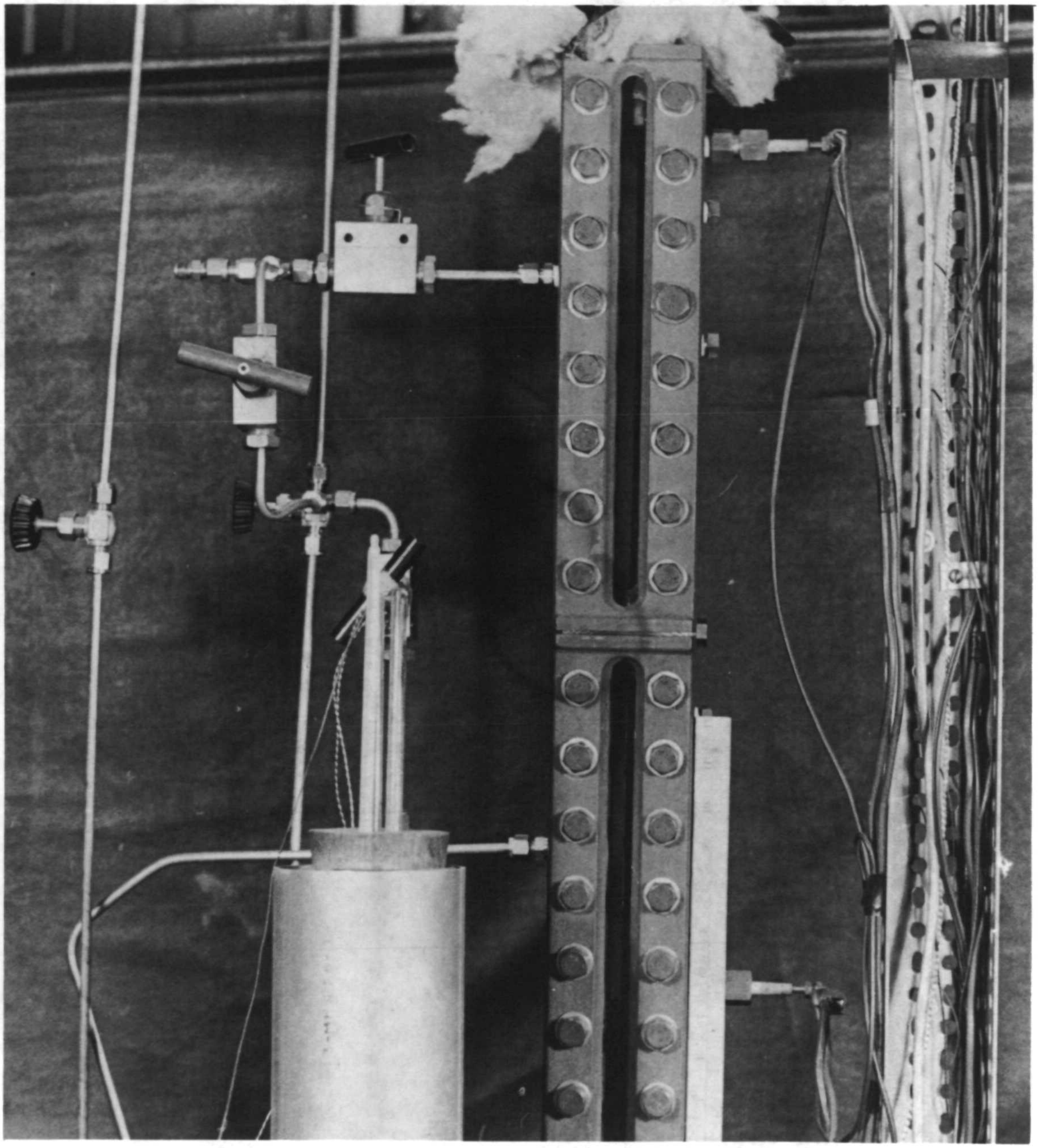

Fig. 4 Section Assembly

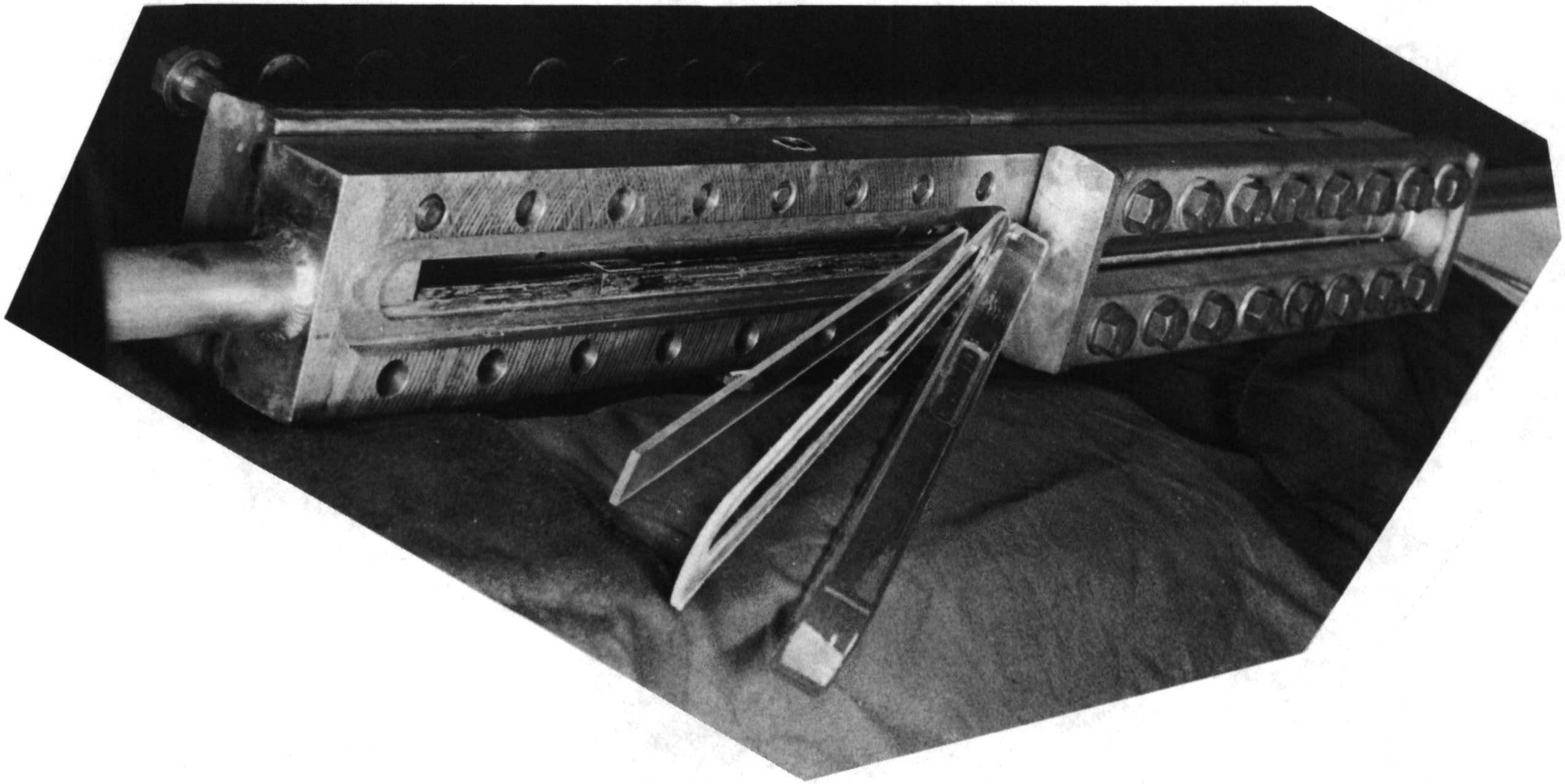

Fig. 5 Fanned view of test section

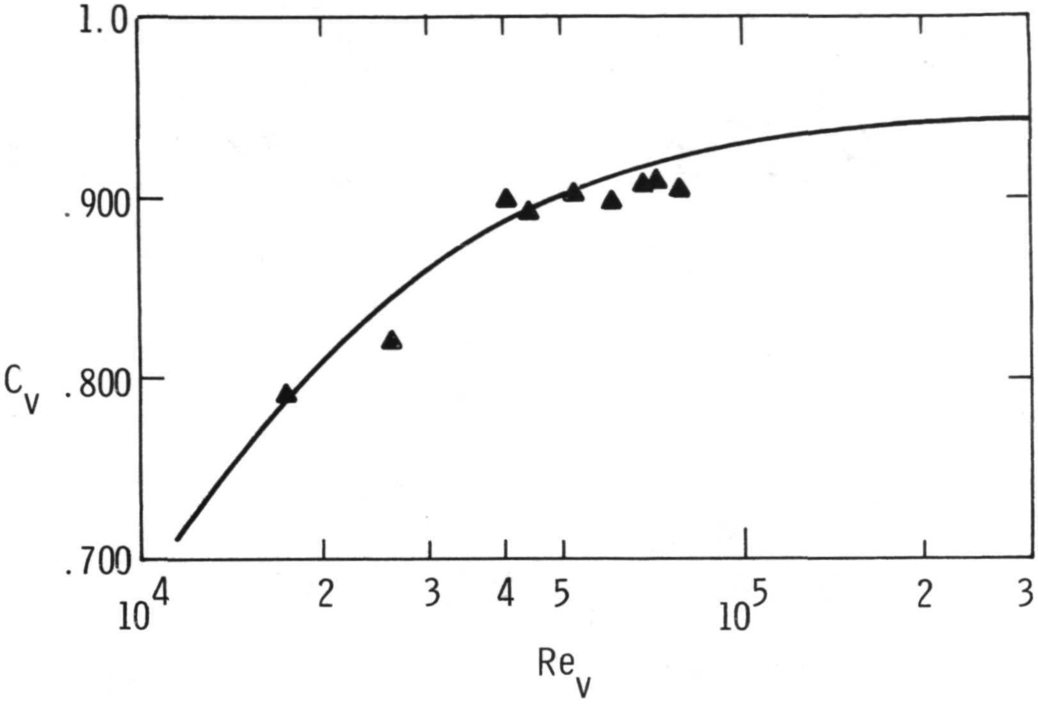

Fig. 6 Venturi calibration

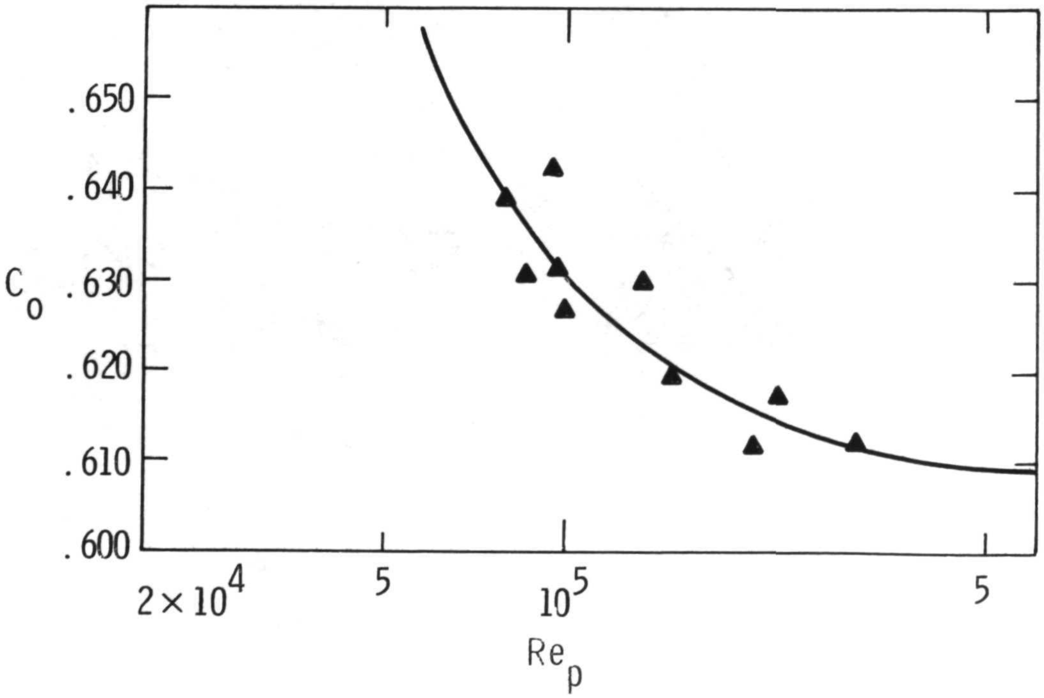

Fig. 7 Orifice calibration

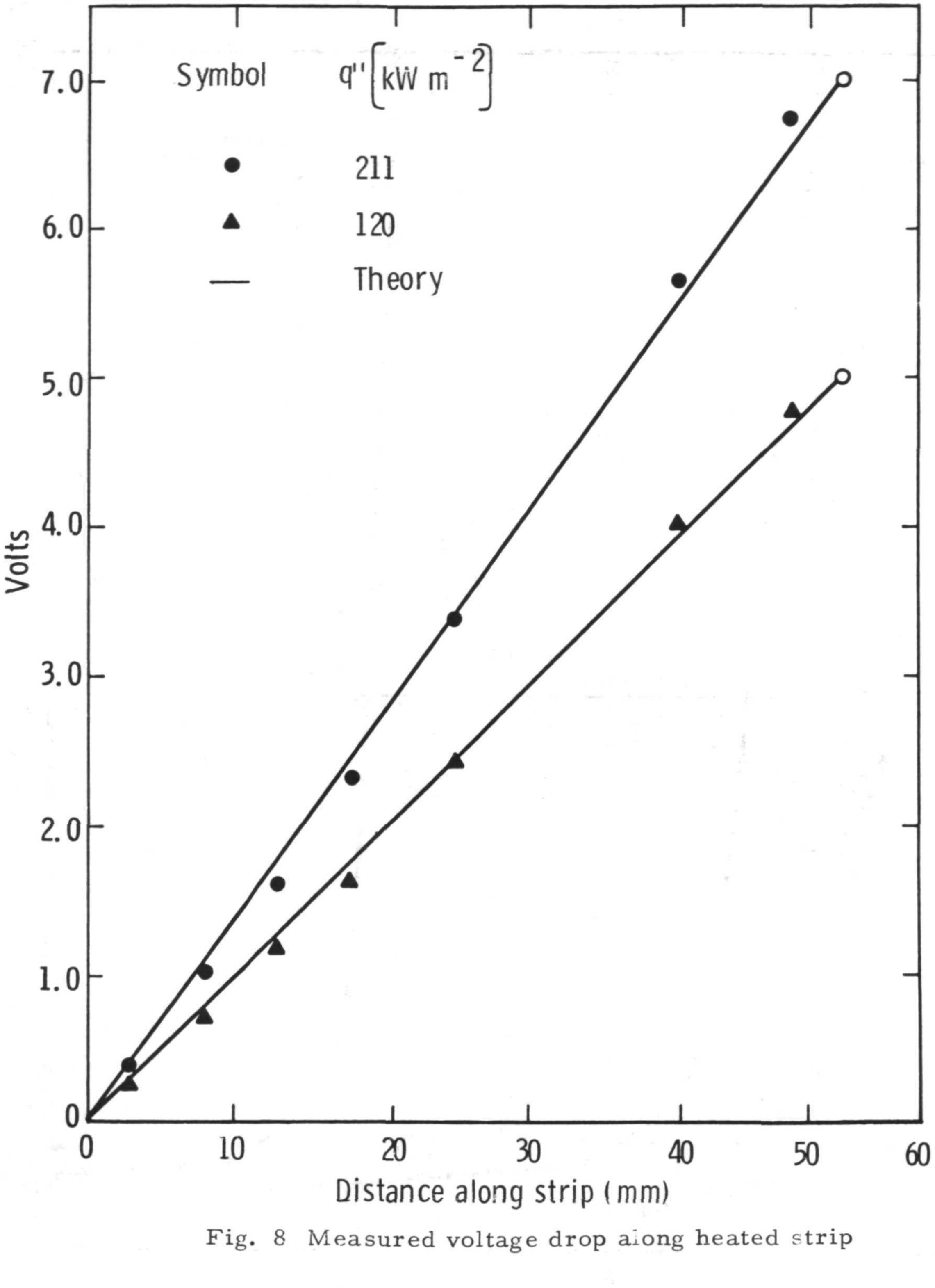

Fig. 8 Measured voltage drop along heated strip

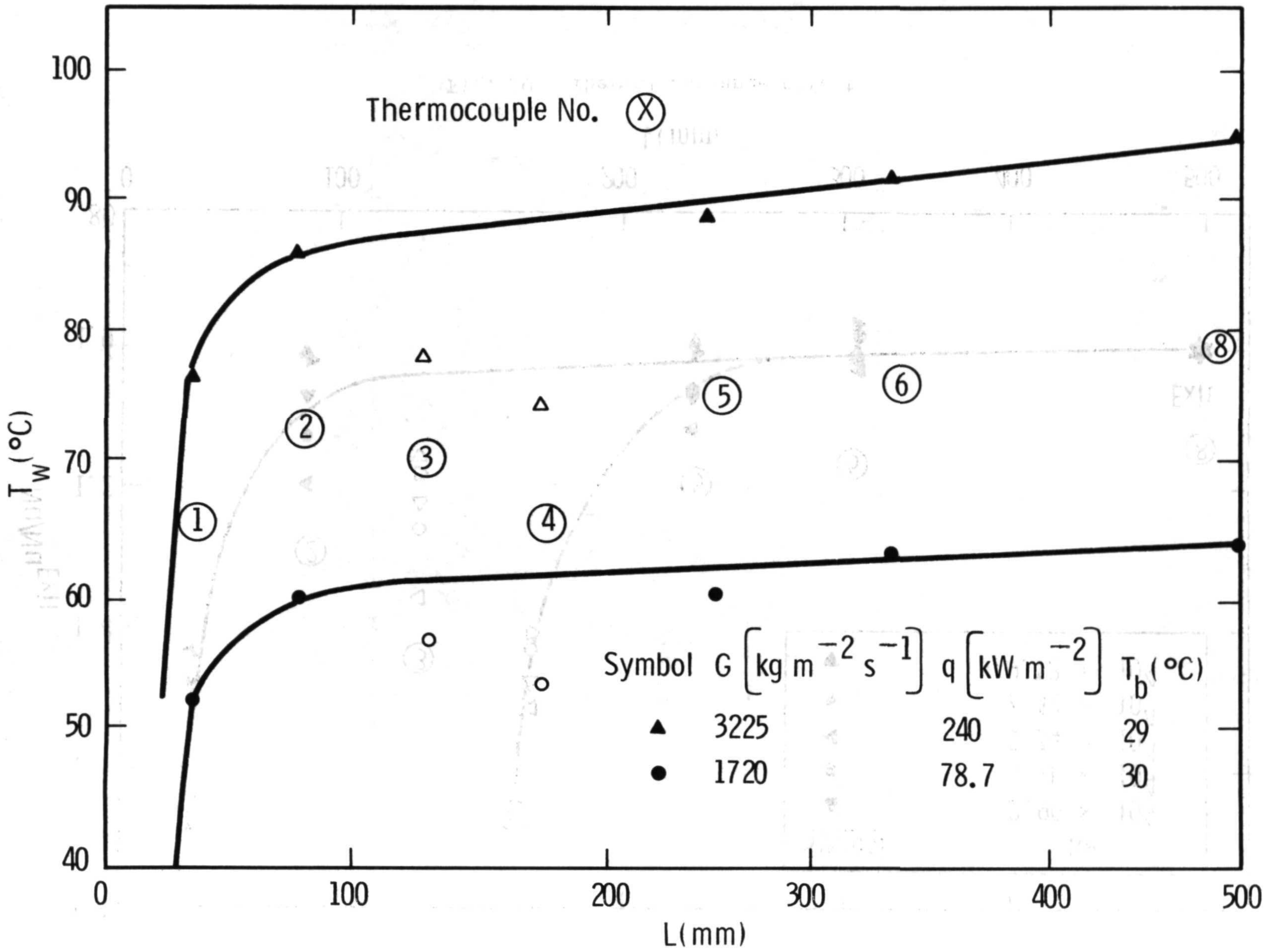

Fig. 9 Forced-convection wall temperature profiles

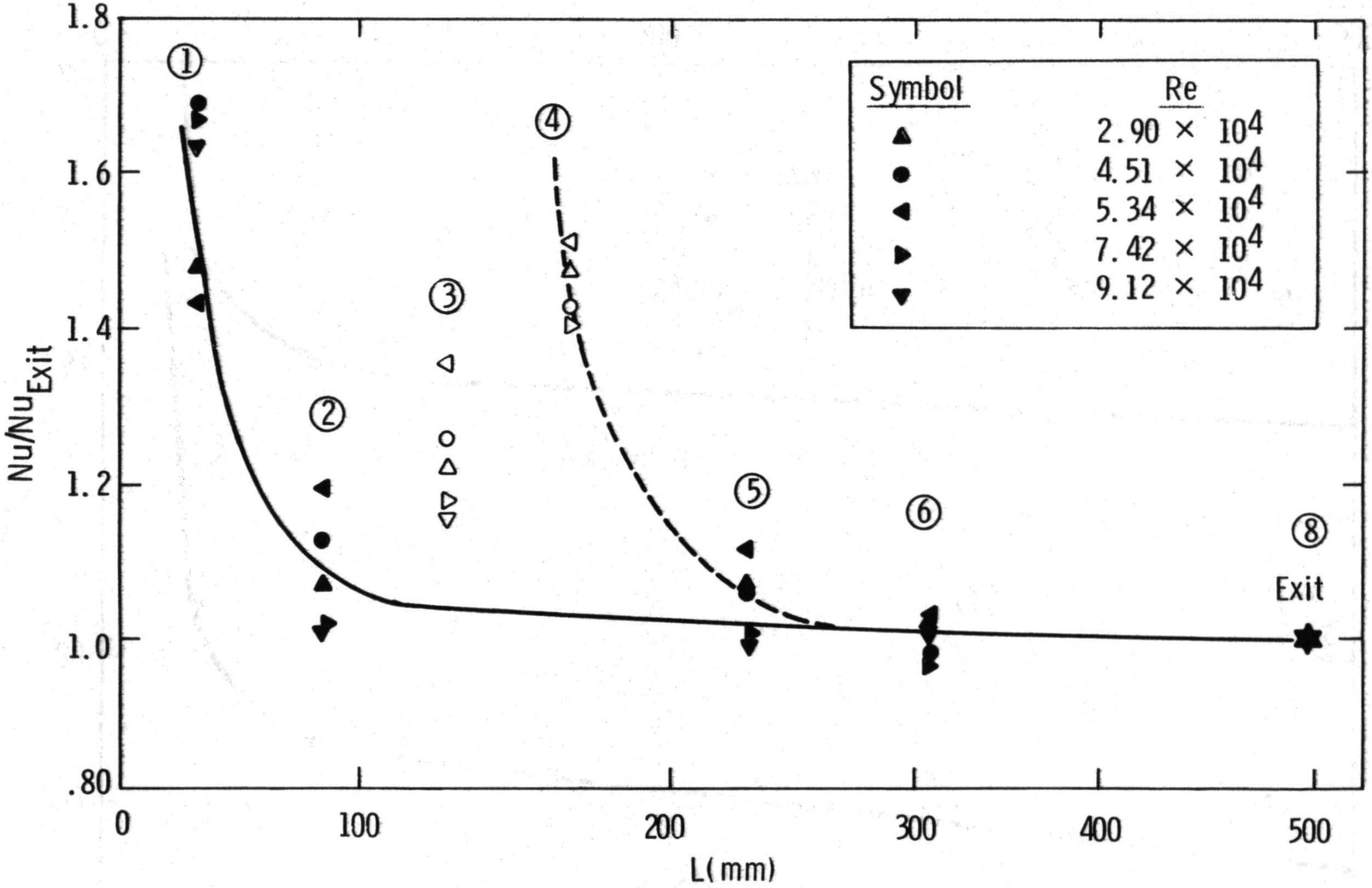

Fig. 10 Thermal entrance effect

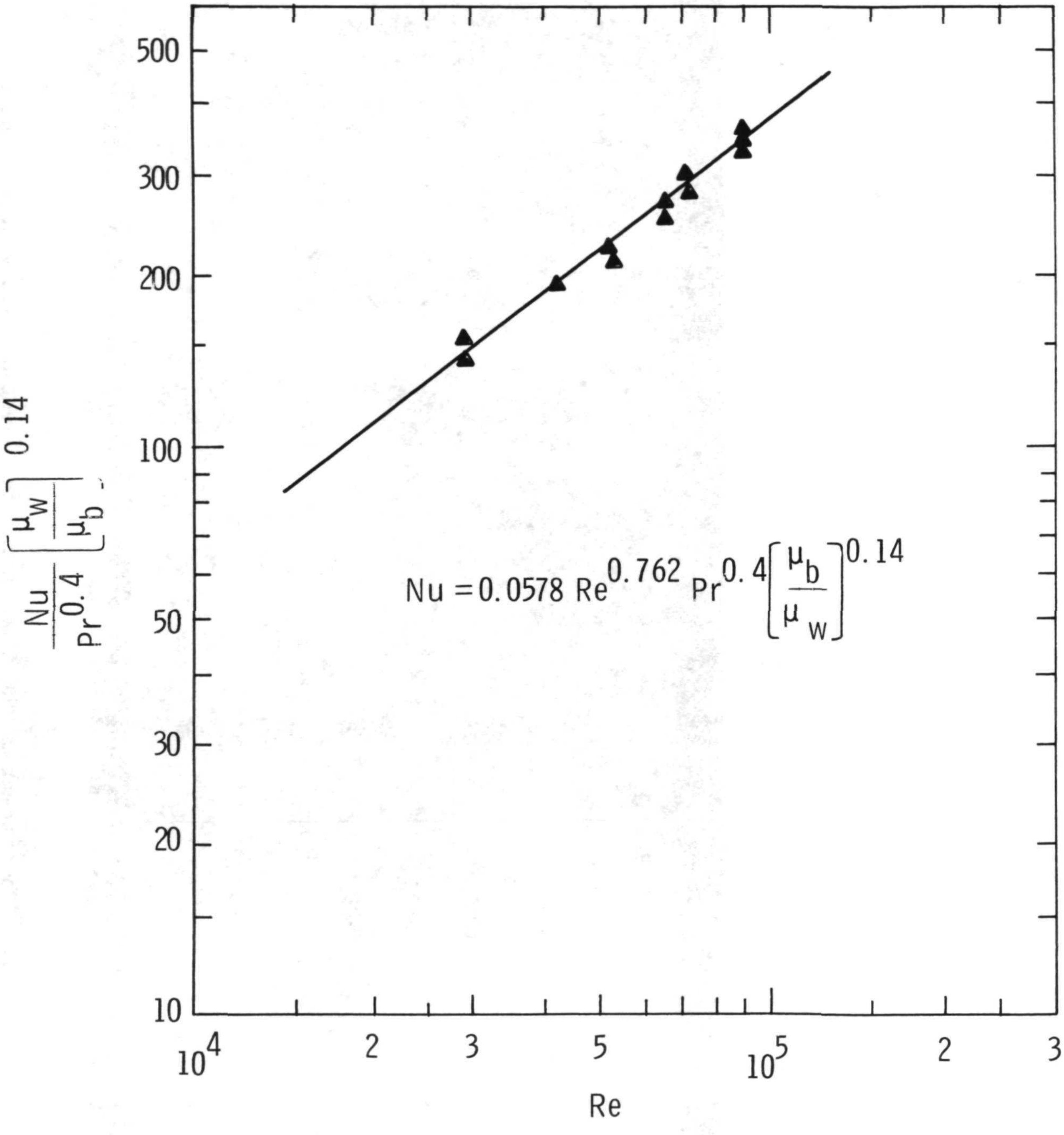

Fig. 11 Forced convection heat transfer correlation

$p = 9.45$ bar

$G = 813$ kg m^{-2} s^{-1}

$\Delta T_{sub} = 31°C$

$q'' = 38.2$ kW m^{-2}

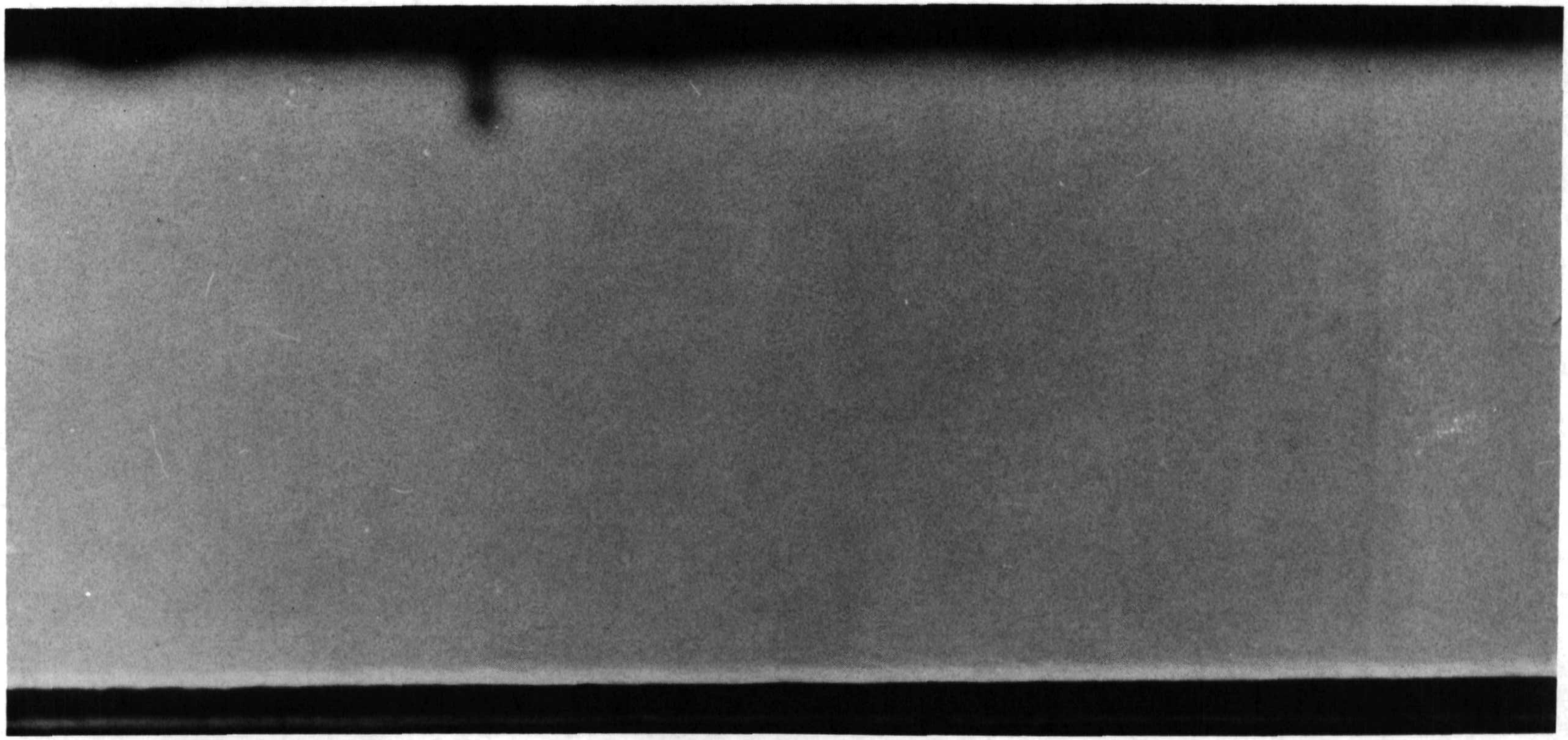

Fig. 12 Photograph of the flow in the test section before bubble inception

Set 1 No. 032017

$p = 9.45$ bar

$G = 813$ kg m^{-2} s^{-1}

$\Delta T_{sub} = 31°C$

$q'' = 53.0$ kW m^{-2}

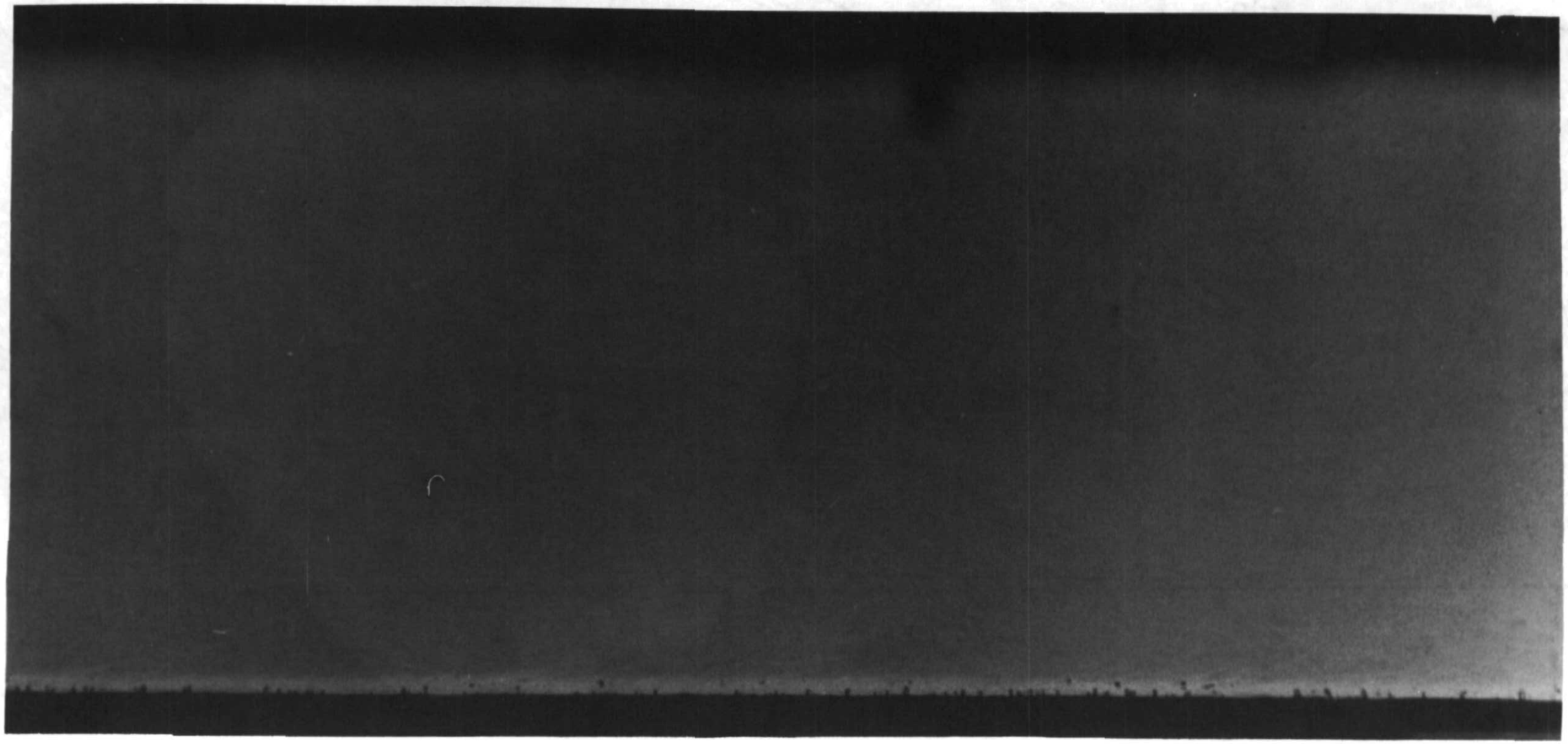

Fig. 13 Photograph of the flow in the test section after bubble inception.

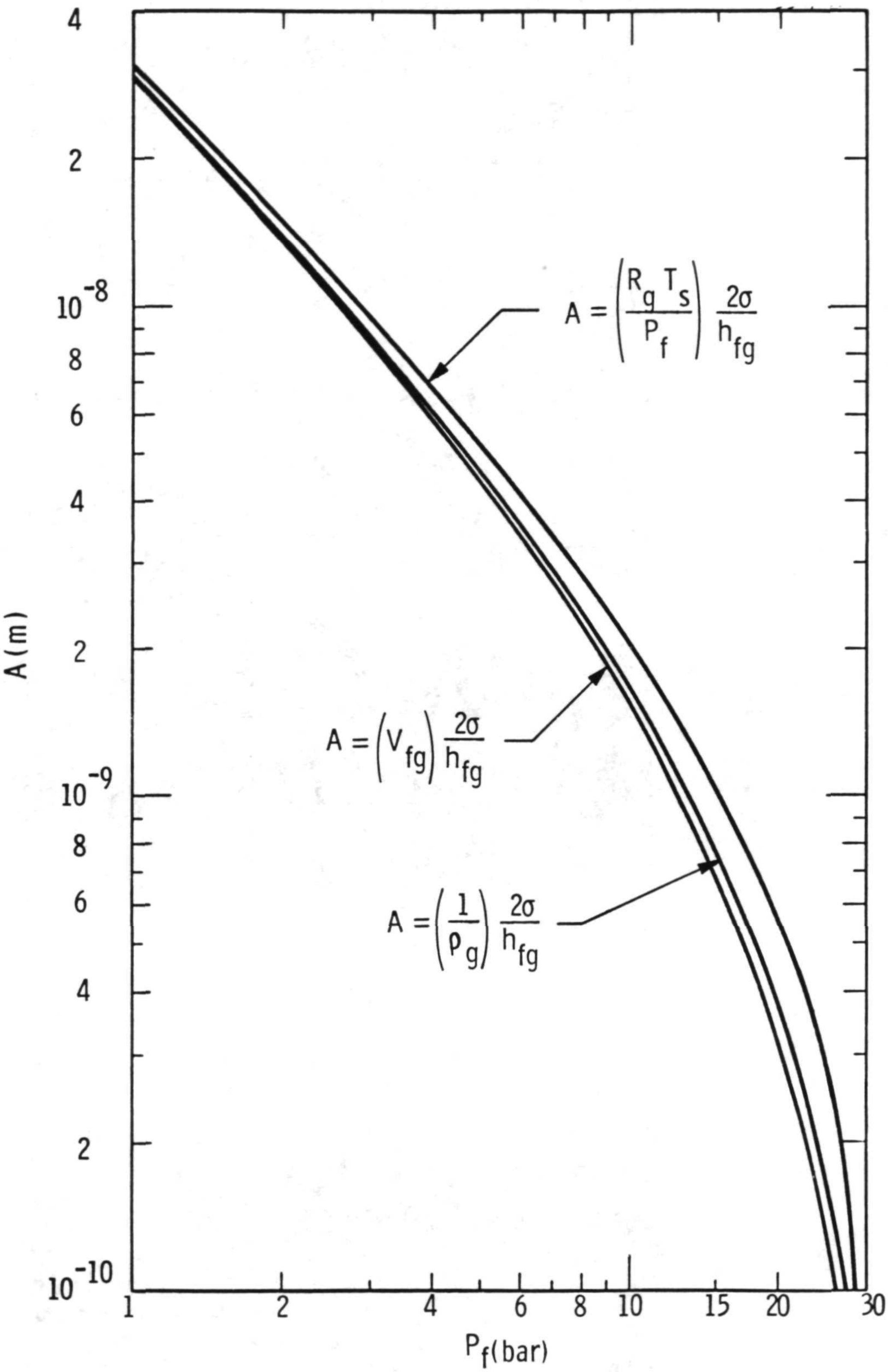

Fig. 14 Variations of the fluid property functions with pressure for R-113

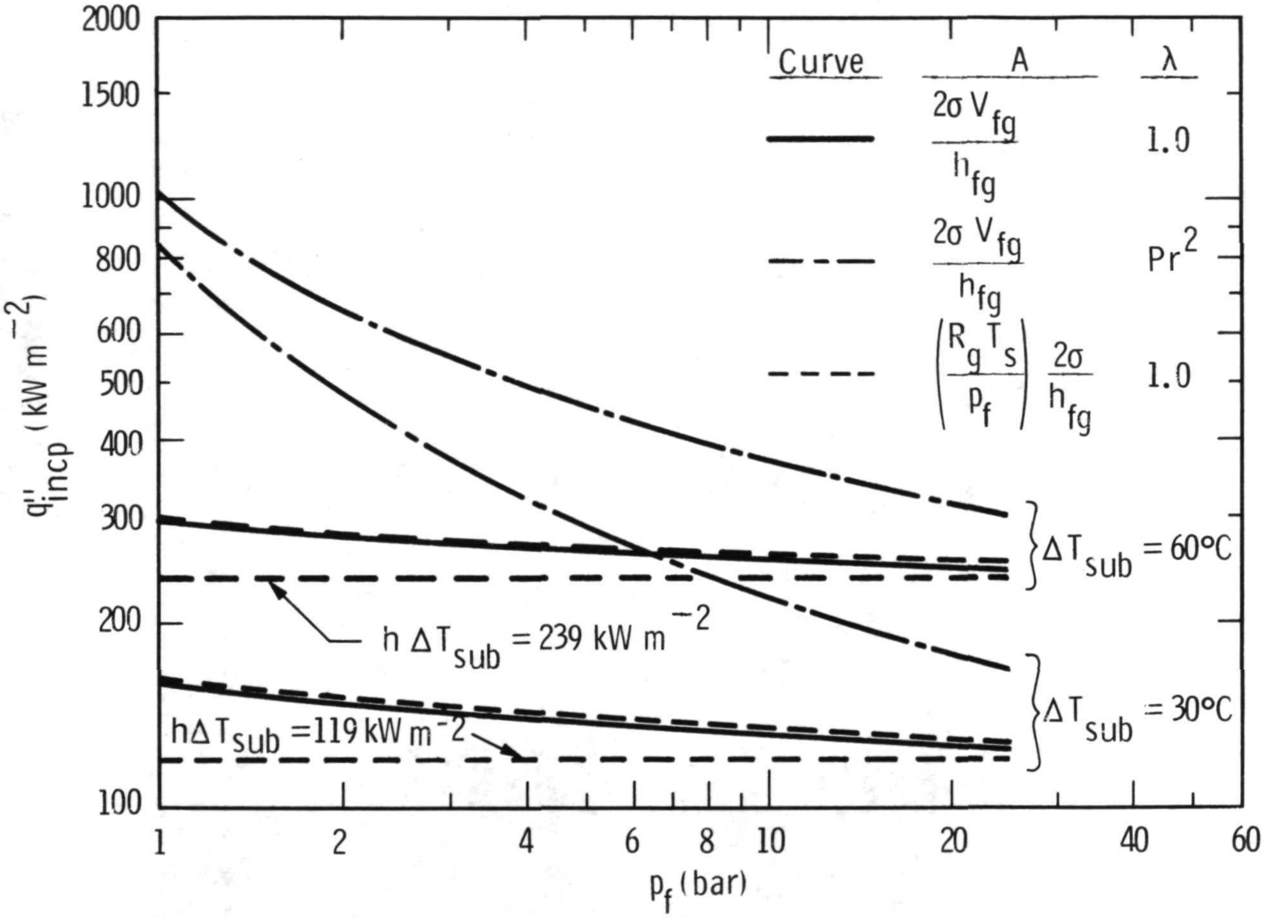

Fig. 15 Theoretical variations of inception heat flux for R-113 with h = 4.00 kW m^{-2} K^{-1}

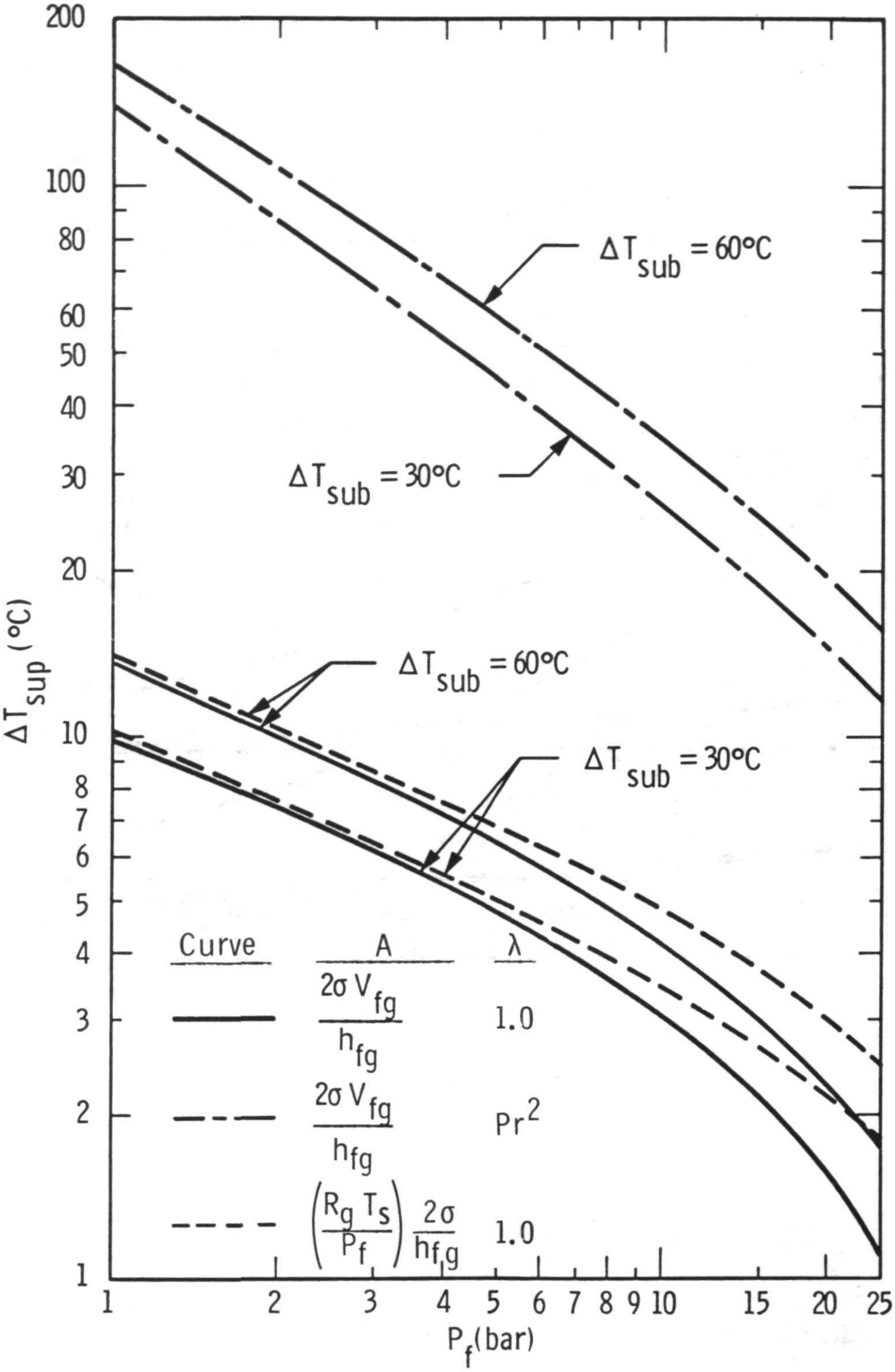

Fig. 16 Theoretical variations of inception wall superheats for R-113 with h = 4.00 K W $m^{-2}K^{-1}$

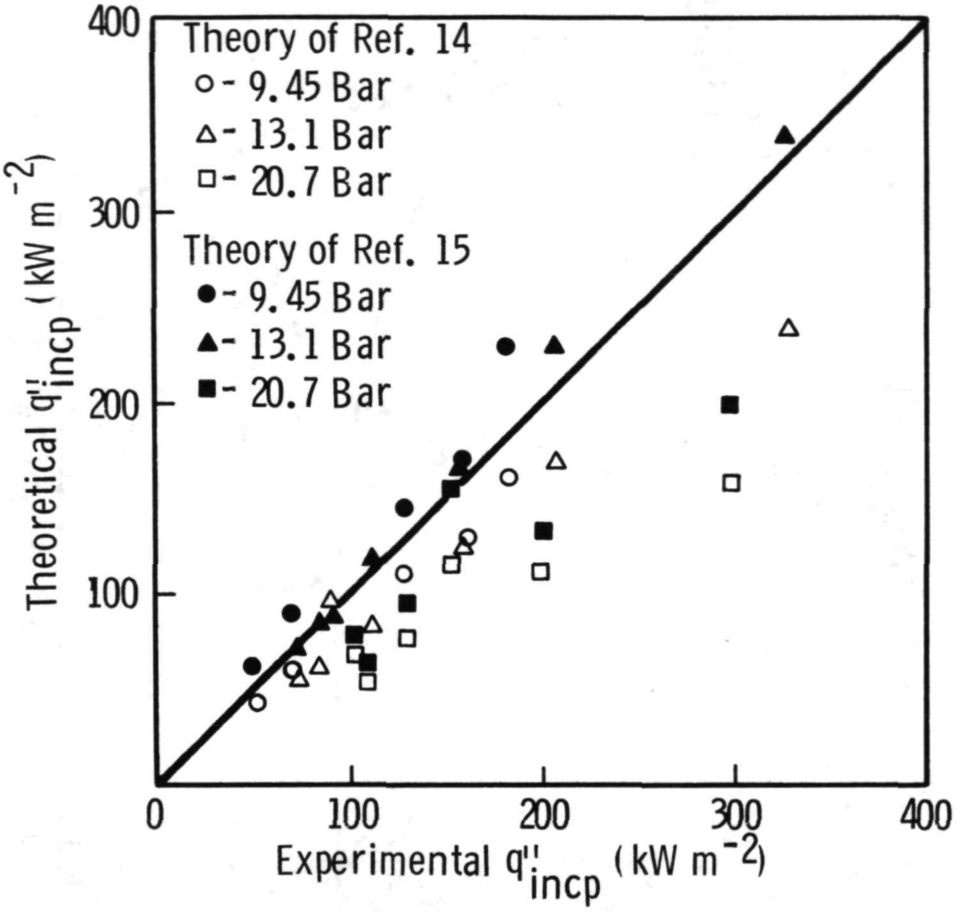

Fig. 17 Comparison of boiling inception theories with experimental data

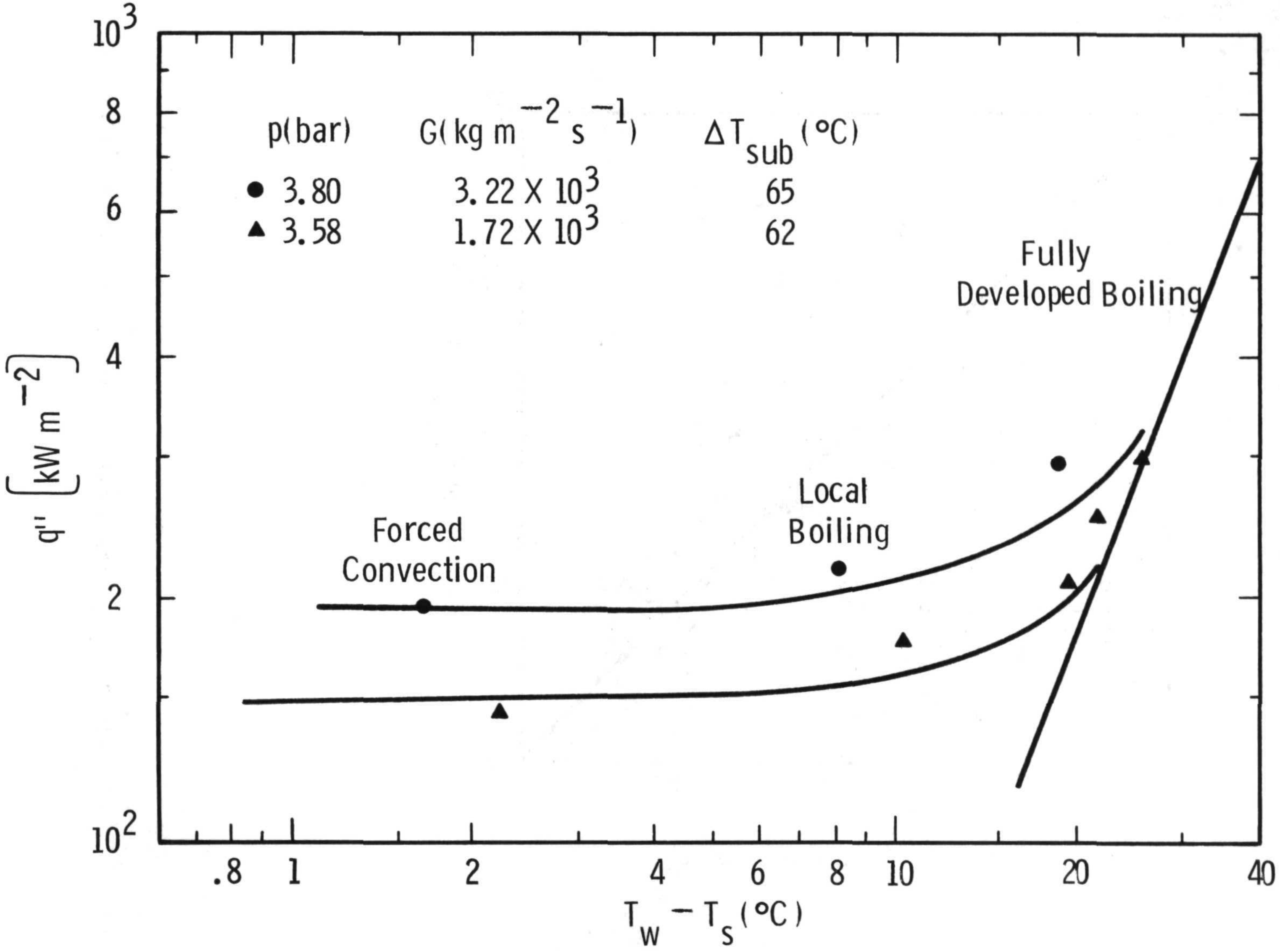

Fig. 18 Forced-convection boiling curve for R-113 at 3.8 bar

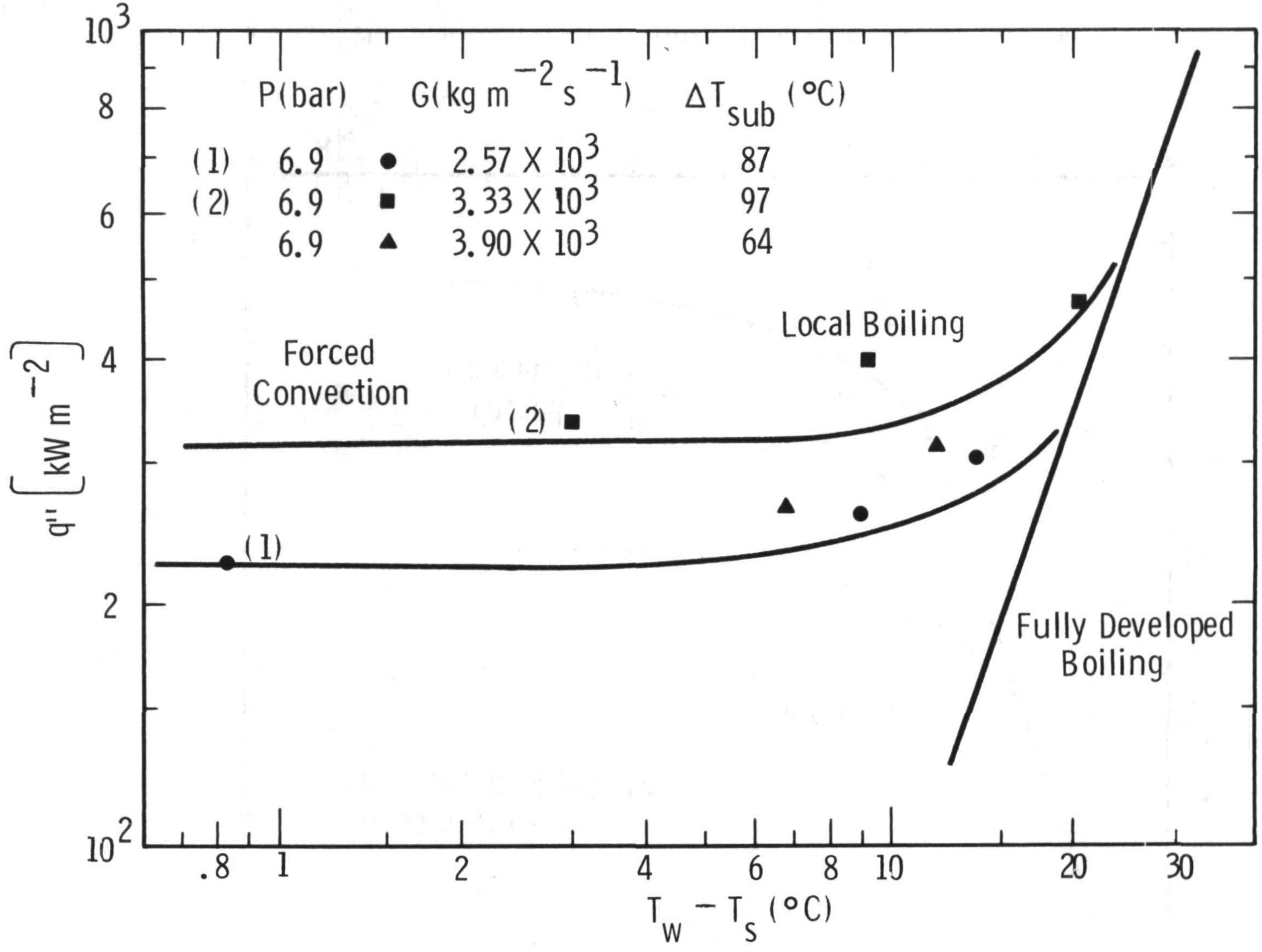

Fig. 19 Forced-convection boiling curve for R-113 at 6.9 bar

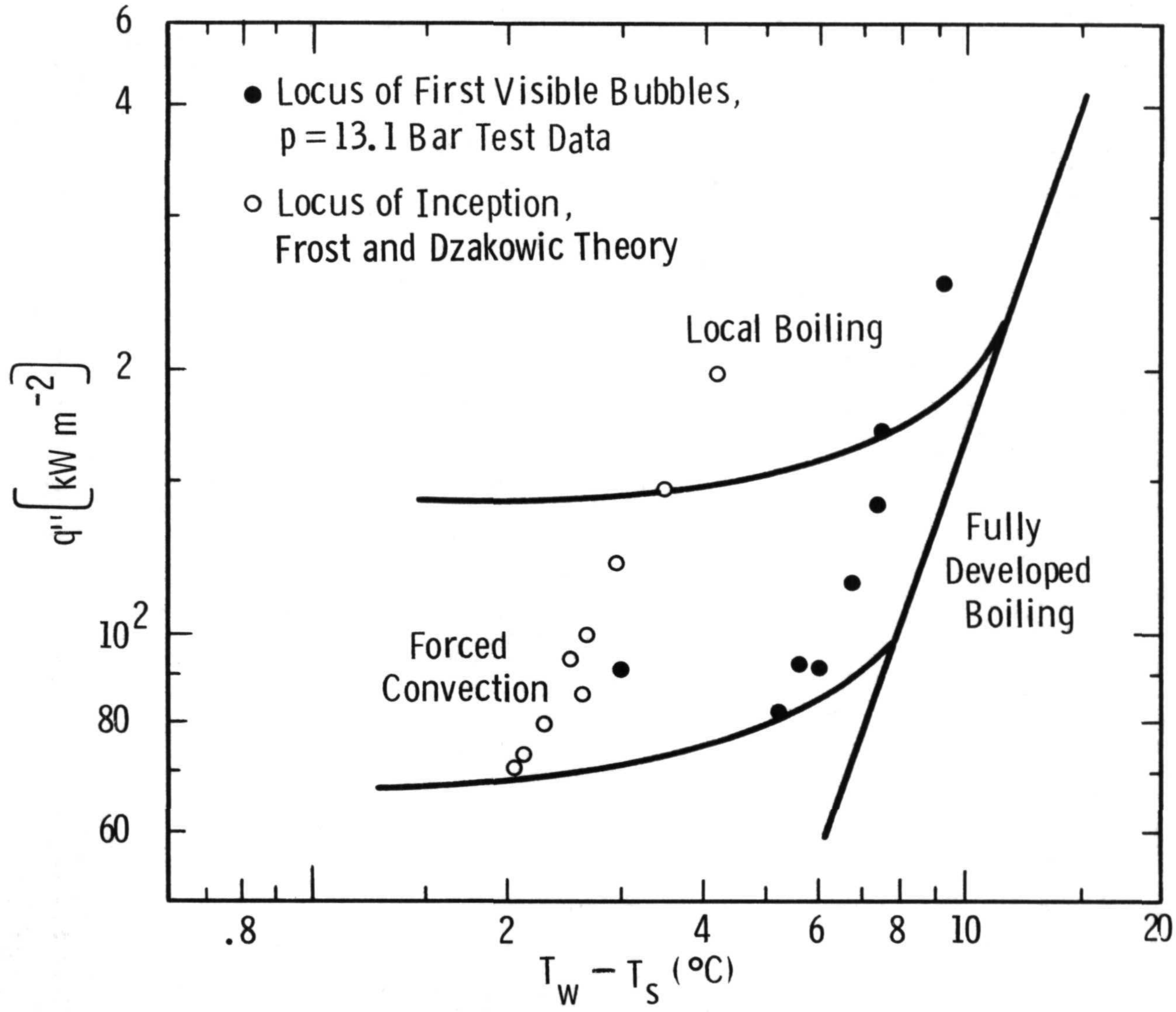

Fig. 20 The locus of first visible bubbles, R-113 and 13.1 bar

NASA-Langley, 1972 — 33 E-7185

NATIONAL AERONAUTICS AND SPACE ADMINISTRATION
WASHINGTON, D.C. 20546

OFFICIAL BUSINESS
PENALTY FOR PRIVATE USE $300

FIRST CLASS MAIL

POSTAGE AND FEES PAID
NATIONAL AERONAUTICS AND
SPACE ADMINISTRATION

U.S.MAIL

NASA 451

POSTMASTER: If Undeliverable (Section 158 Postal Manual) Do Not Return

---

> *"The aeronautical and space activities of the United States shall be conducted so as to contribute . . . to the expansion of human knowledge of phenomena in the atmosphere and space. The Administration shall provide for the widest practicable and appropriate dissemination of information concerning its activities and the results thereof."*
>
> —NATIONAL AERONAUTICS AND SPACE ACT OF 1958

NASA SCIENTIFIC AND TECHNICAL PUBLICATIONS

TECHNICAL REPORTS: Scientific and technical information considered important, complete, and a lasting contribution to existing knowledge.

TECHNICAL NOTES: Information less broad in scope but nevertheless of importance as a contribution to existing knowledge.

TECHNICAL MEMORANDUMS: Information receiving limited distribution because of preliminary data, security classification, or other reasons.

CONTRACTOR REPORTS: Scientific and technical information generated under a NASA contract or grant and considered an important contribution to existing knowledge.

TECHNICAL TRANSLATIONS: Information published in a foreign language considered to merit NASA distribution in English.

SPECIAL PUBLICATIONS: Information derived from or of value to NASA activities. Publications include conference proceedings, monographs, data compilations, handbooks, sourcebooks, and special bibliographies.

TECHNOLOGY UTILIZATION PUBLICATIONS: Information on technology used by NASA that may be of particular interest in commercial and other non-aerospace applications. Publications include Tech Briefs, Technology Utilization Reports and Technology Surveys.

Details on the availability of these publications may be obtained from:

SCIENTIFIC AND TECHNICAL INFORMATION OFFICE

NATIONAL AERONAUTICS AND SPACE ADMINISTRATION
Washington, D.C. 20546